Engineering Geology 114 (2010) 278–297

Contents lists available at ScienceDirect

Engineering Geology

journal homepage: www.elsevier.com/locate/enggeo

Hazard investigation of the Portillo Rock Avalanche site, central Andes, Chile, using an integrated field mapping and numerical modelling approach

D. Welkner [a,b], E. Eberhardt [a,*], R.L. Hermanns [c]

[a] Geological Engineering/EOS, University of British Columbia, Vancouver, B.C., Canada
[b] BGC Engineering Inc., 500-1045 Howe St., Vancouver, BC, Canada
[c] Geological Survey of Norway, International Centre for Geohazards, Trondheim, Norway

ARTICLE INFO

Article history:
Received 2 February 2010
Received in revised form 6 May 2010
Accepted 12 May 2010
Available online 24 May 2010

Keywords:
Rockslide hazard assessment
Cosmogenic dating
Stress-controlled failure
Trigger mechanism analysis
Runout analysis
Chilean Andes

ABSTRACT

This paper reports a detailed rock slope hazard investigation of the Portillo Rock Avalanche site located in the rugged mountains of the Andean Cordillera of central Chile. The site is important as it lies along the International Santiago–Mendoza Highway Corridor connecting Chile and Argentina, and a major ski resort is located on its deposits. A number of large lobate-shaped diamicton deposits were mapped and dated by cosmogenic nuclides (^{36}Cl), with the results showing that they correspond to two significant prehistoric rockslide events. An integrated field mapping and numerical modelling investigation was subsequently carried out to assess the threat posed to the area by further rocksliding activity. Distinct-element modelling was used to back analyze the failure mechanism and identify the geological model that best reproduced the Portillo Rock Avalanche failure surface. Results show that a stress-controlled failure at the toe of the slope followed by sliding along volcaniclastic bedding was the likely failure mechanism. A 3-D dynamic runout analysis was carried out to back analyze which combinations of rheologies, material properties and rockslide sequencing were best able to reproduce the current distribution of rockslide deposits. Results indicate that two separate sliding events originating from different sources had occurred, with each involving different combinations of frictional and Voellmy rheologies depending on the level of entrainment that occurred along each travel path.

Insights gained from the back analysis were then used to carry out a forward analysis to assess the potential for a recurring major rockslide under several different triggering scenarios. Results suggest that a low probability M 7.8 earthquake would be required to trigger another rockslide from the original source area. The rock slope was otherwise found to be stable, even following high precipitation events. Nevertheless, runout simulations for the estimated large-magnitude earthquake-triggered rockslide volume showed that for both a highly frictional and non-saturated path (i.e. dry season) and a snow covered path (winter), the leading edge of the flow would override part of the International Santiago–Mendoza Corridor with the debris coming to rest in a flat-lying area in the upper part of the valley. Overall, the results from this integrated hazard assessment suggest that the hazard level is low.

1. Introduction

Analysis of massive rock slope failures and subsequent motion of rapid rockslide runouts is a challenging task given the difficulty in determining the processes and circumstances involved. This task is even more complex when dealing with prehistoric rock avalanches due to the need for paleo-landscape reconstruction and knowledge of the pre-failure conditions. In most cases, only approximations of reality can be provided based on judgment and experience due to geologic uncertainty and the inherently variable nature of rock.

In the rugged mountains of the Andean Cordillera of central Chile, close to the Chile–Argentina border (Fig. 1a), a number of large lobate-shaped diamicton deposits near Inca Lake along the Caracoles Range (Fig. 1b) have been previously identified as moraines owing to their detrital characteristics (Caviedes and Paskoff, 1975). However, subsequent detailed mapping, including textural, compositional, and stratigraphic relations to the geomorphic setting, yielded no clear evidence of moraines, and the deposits have since been reinterpreted as belonging to a prehistoric rockslide (Rivano et al., 1993; Godoy, 1994). This reinterpretation changes the assessment of the hazard posed by future rockslide events at the site, which encompasses the Santiago–Mendoza International Highway Corridor and the Portillo Ski Resort, from negligible (where the deposits were assumed to be of glacial origin), to possible.

* Corresponding author. Earth and Ocean Sciences, 6339 Stores Rd., University of British Columbia, Vancouver, BC, Canada V6T 1Z4. Tel.: +1 604 827 5573; fax: +1 604 822 6088.
E-mail address: erik@eos.ubc.ca (E. Eberhardt).

0013-7952/$ – see front matter © 2010 Elsevier B.V. All rights reserved.
doi:10.1016/j.enggeo.2010.05.007

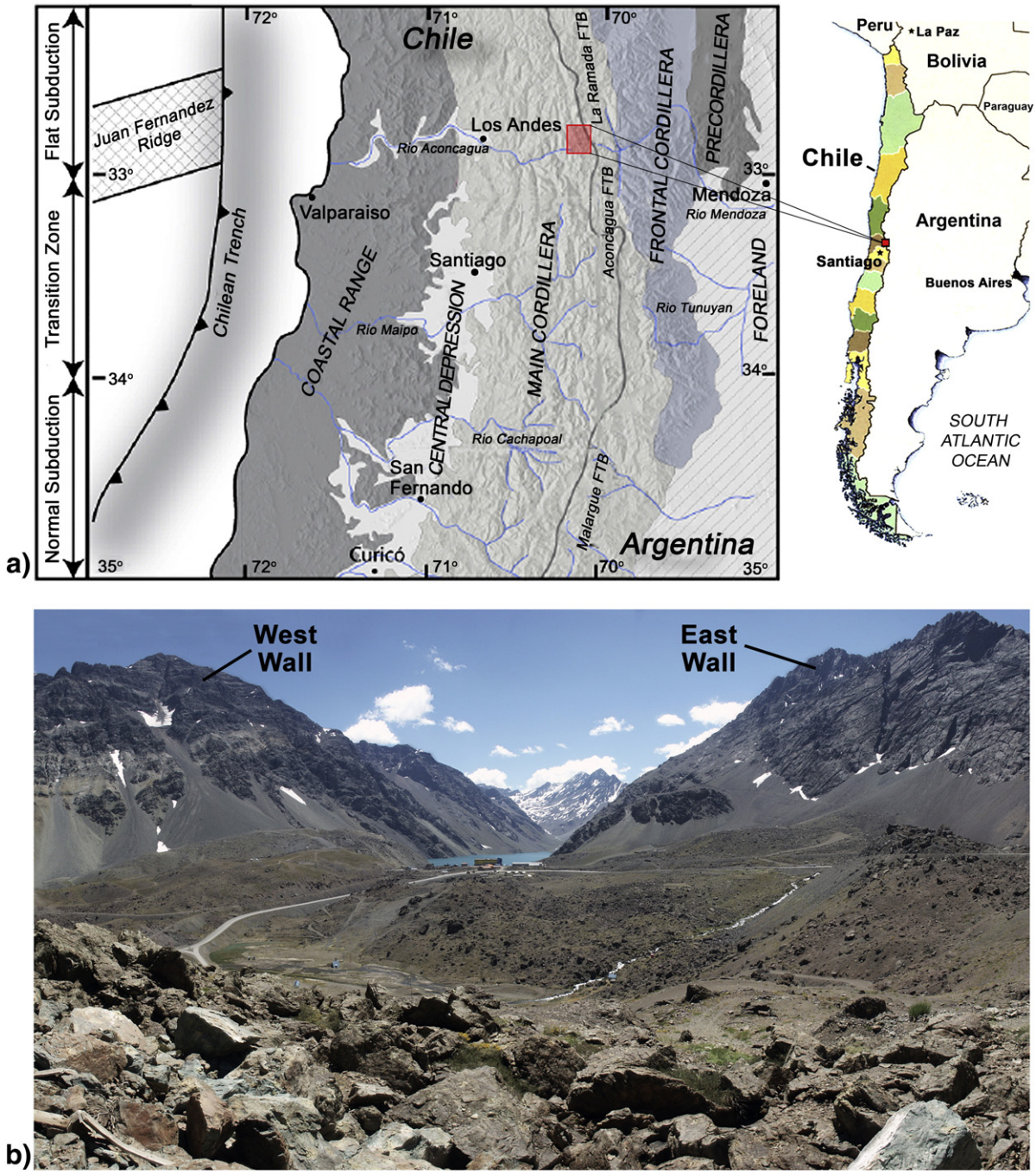

Fig. 1. a) Tectonic map of the Chilean Andes highlighting the study area east of Los Andes (after Giambiagi and Ramos, 2002), and relationship to location map of Chile; b) Panoramic photo of the Portillo rockslide deposits looking north, with Inca Lake and the Portillo Ski Resort in the background.

This paper reports the findings of a detailed investigation into the mapping and reinterpretation of the source of these deposits, and a subsequent rock slope hazard investigation into the failure mechanism, volume and runout characteristics of the prehistoric events. Insights gained through the back analysis are then used to calibrate and constrain a series of forward analyses used to assess the hazard potential of a reoccurring major rockslide at the Portillo site.

2. Field investigation and engineering geology of the study area

The study area is located near Portillo, Chile, on the western flank of the central Andean Cordillera between 32°S and 33°S and approximately 70°05′W (Fig. 1a). In this region the average altitude is 4000 m.a.s.l., with summit altitudes exceeding 6000 m.a.s.l. The regional geological setting involves an extensional volcano-tectonic basin that developed between the middle to late Eocene and Oligocene (Godoy et al., 1999; Charrier et al., 2002) on the western (i.e. Chilean) side of the Andean Cordillera. This basin was developed under extensional conditions and underwent subsequent tectonic inversion (Charrier et al., 2002) in response to the extreme compression that initiated around 26 ± 1 Ma with the beginning of the orthogonal convergence of the Nazca and South American plates (Tebbens and Candie, 1997).

2.1. Tectonic setting and seismicity

The regional tectonic setting is characterized by the subduction of the oceanic Nazca Plate beneath the continental South American

lithosphere along the Chilean trench (Fig. 1a). The subduction zone forms an east-dipping seismic zone, with interplate underthrusting earthquakes (M>8) occurring with return periods in the order of 80 to 130 years for central Chile (Barrientos et al., 2004). Beneath central Chile and western Argentina (28°S–33°S), where the study area is located, the subducted plate is sub-horizontal, with a dip angle of less than 10° that extends east for hundreds of kilometres at a depth of approximately 100 km before resuming its downwards trend (Cahill and Isacks, 1992). Along this segment, most of the earthquakes are compressional with moderate magnitude and depth focus of ~80 km (Pardo et al., 2002; Barrientos et al., 2004), although very shallow (0–20 km) damaging earthquakes ($5.9 \leq M \leq 6.9$) have also been recorded in the area (Lomnitz, 1961; Barrientos et al., 2004; Sepulveda et al., 2008). It is believed that these shallow events are produced by the deformation of the overriding continental plate in response to the differential coupling that exists in the region due to along-strike variations in the dip angle of the Nazca Plate. Recent studies of large rockslides in the central Andean Cordillera suggest that shallow seismicity is a possible triggering mechanism for the numerous mass wasting events that characterize the regional morphology (Antinao and Gosse, 2009).

2.2. Geology and geomorphology

Mapping of the rockslide deposit(s) and potential source area(s) was carried out over several campaigns using conventional mapping techniques aided by air photos, photogrammetry, cosmogenic nuclide dating, and terrestrial laser scanning (LiDAR). Fig. 2 shows the geological map developed for the study area using the 1:250,000 bedrock geology map of Rivano et al. (1993) as a base map. The bedrock corresponds to late Eocene to early Miocene andesitic lavas and volcaniclastic and sedimentary bedded rocks.

Along the east wall of the valley (the Caracoles Range), the bedding forms a dip slope (i.e. bedding parallel to the slope surface) that dips between 50–60°W towards the valley (see Figs. 1b and 2). At the toe of the slope, a back-thrust was mapped which structurally separates west-dipping rocks of the hanging wall from east-dipping rocks of the footwall, with bedding below the thrust fault dipping

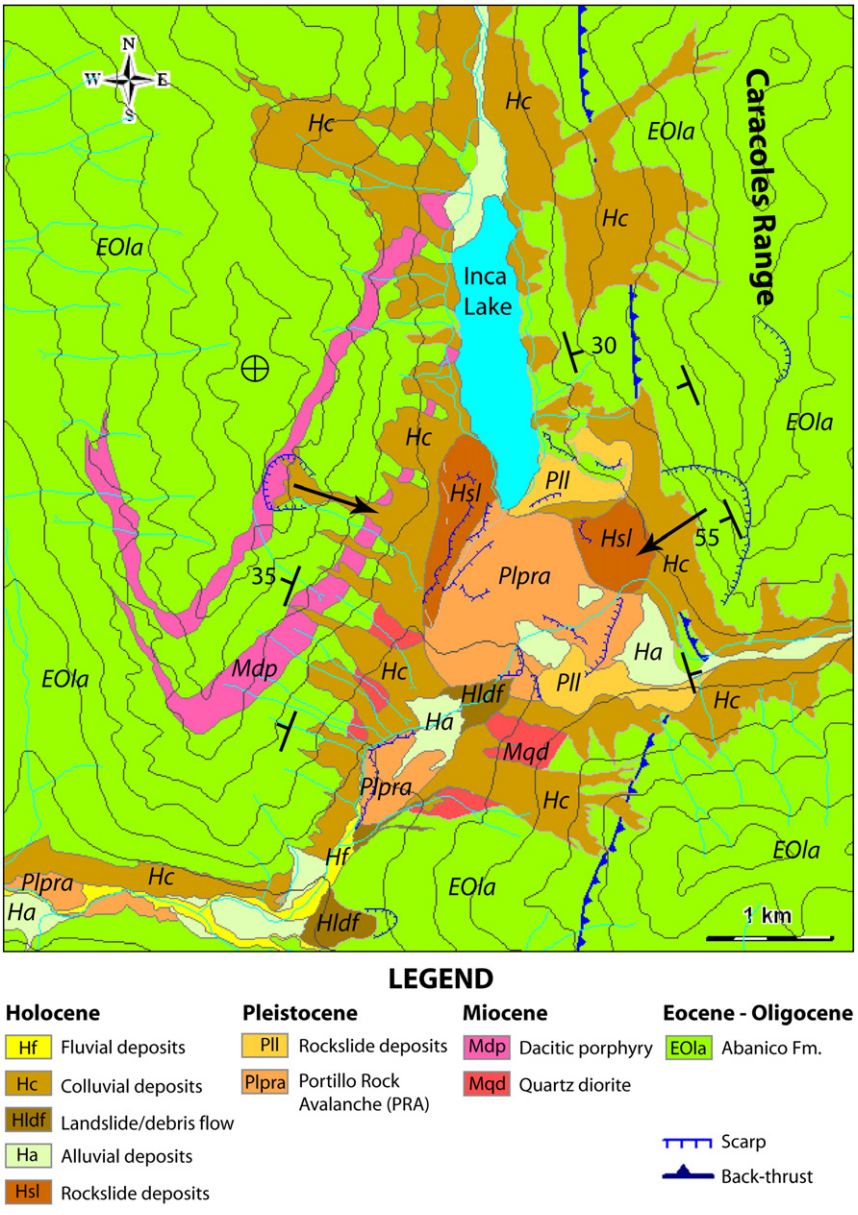

Fig. 2. Geological map of the study area using the 1:250,000 map of Rivano et al. (1993) as a base map.

approximately 30°E into the slope. It is suggested here that the thrust fault that outcrops in the study area originated during a compressional episode *ca.* 10–8 Ma, which is believed to be responsible for the uplift of the range and its associated large-scale thrusting (Ramos et al., 2004) observable to the east of the study area (Godoy 2002; Yañez et al., 2002). On the west side of the valley, the volcaniclastic rocks dip roughly 35°W gradually reaching a sub-horizontal position towards the top of the west wall (Figs. 1b and 2).

The bedrock is occasionally intruded by minor stocks and sills (Mqd and Mdp in Fig. 2, respectively) which commonly leave an imprint of altered and fractured bedrock around the intrusive contact. Localized relationships between these weakness zones and initiation zones for minor rockfalls can be recognized in the study area and its surroundings.

The geomorphology of the valley is marked by barren, boulder-covered lobes or ridges involving a number of rockslide deposits. Chief amongst these are the deposits from a large rock avalanche, the Portillo Rock Avalanche (Plpra in Fig. 2), projected to have originated from the east wall dip slope (Fig. 1b). These were mapped as involving different granulometric domains (proximal, medial and distal) according to their relative position from the east wall. The proximal domain is comprised of large angular blocks up to 750 m^3 in size (Fig. 3a), that are similar to the lithology of the Abanico Formation (Fig. 2) characterized by distinctive reddish volcanic breccias with large (>5 cm) chlorite and epidote-rich nodules (Fig. 3b). The fragments often show fault striations on their free surfaces. Down the valley, the deposit appears to follow the paleo-topography which could be compared to that of a glacially carved steep undulating valley floor. Abrupt faces of coarse debris where the valley steepens and narrows, or plateaus more recently covered by alluvial sediments (Ha in Fig. 2) where the valley floor flattens are common features. These medial (or transitional) deposits are finer and better graded, with the coarse portion made up of angular cobbles and coarse gravel. The lithology of the fragments is similar to the one described for the upper part of the valley, while the matrix, made up of sand and silt, is rich in feldspar, quartz, pyroxene, and epidote. At the distal edge of the rockslide deposit, the material takes the form of hummocky terrain (Fig. 3c). The base of the deposit is not exposed.

It is likely that the major impact of the Portillo Rock Avalanche on the prehistoric landscape was the obstruction of the N–S valley drainage and the formation of Inca Lake. Field observations of the deposit in the upper segment of the valley strongly support this hypothesis.

Contiguous with the Portillo Rock Avalanche deposits are other rockslide deposits (Pll in Fig. 2). Based on their stratigraphic position and relative relation with the other deposits, they were assigned to the Pleistocene. Of these, only the northern deposit has a recognized source scarp, while the source of the southern deposit is unclear.

A set of younger rockslide deposits were also identified, which are characterized by two distinct deposits found along the east and west margins of the valley overlaying the Portillo Rock Avalanche deposits (Hsl in Fig. 2). The eastern deposits are made up of cobbles and boulders of andesitic lavas and breccias with some gravel and sand-rich matrix. Even though its scarp is not clearly identifiable, it is evident that it came from the eastern wall aided by the slope-parallel westward dipping bedding planes. The west lobe deposit is made up of self-supported angular boulders and blocks of porphyritic andesitic lavas, lapilli tuffs, fine grained andesites and white dacitic porphyry (Fig. 4). The dacitic blocks come from a sill that outcrops only in the western wall and intrudes the volcaniclastic rocks of the Abanico Formation (Fig. 2).

2.3. Cosmogenic nuclide dating

With a number of different deposits in the Portillo study area being identified as belonging to multiple prehistoric rockslides, based on the identification of different source areas, superposition of the deposits and, when possible, distinct lithologies, surface exposure dating by Terrestrial Cosmogenic Nuclides (TCN) was used to help further constrain the chronology of rockslide events. This novel method helped to provide absolute dates for the deposits.

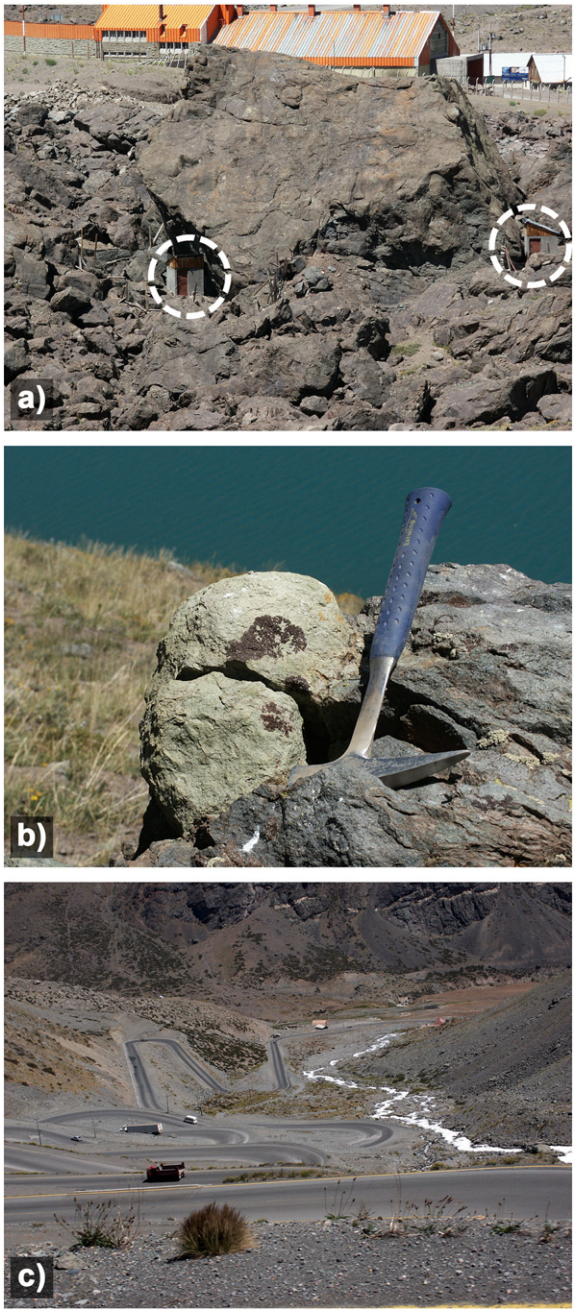

Fig. 3. Photos of the Portillo Rock Avalanche deposit along its path. a) Proximal deposit involving large rock blocks. Note the ski sheds highlighted by white dashed circles for scale (approximate height = 3 m). b) Large epidote-rich nodule, characteristic of the volcanic breccias of the Abanico Formation. c) Switch-back of the Santiago–Mendoza International Highway Corridor as it traverses the distal deposits of the Portillo Rock Avalanche with the hummocky terrain in the distance marking the outer margins of the deposit (see Fig. 5).

TCN dating is based on the formation of chlorine-36 nuclides (^{36}Cl) through two production avenues: spallation of ^{40}Ca and ^{39}K under cosmic ray bombardment, and neutron activation of ^{35}Cl. The rates of accumulation are proportional to the cosmic ray flux and concentration of target nuclides in the surface material. Evidence of cosmic ray spallation is evidence that the material in question has been exposed

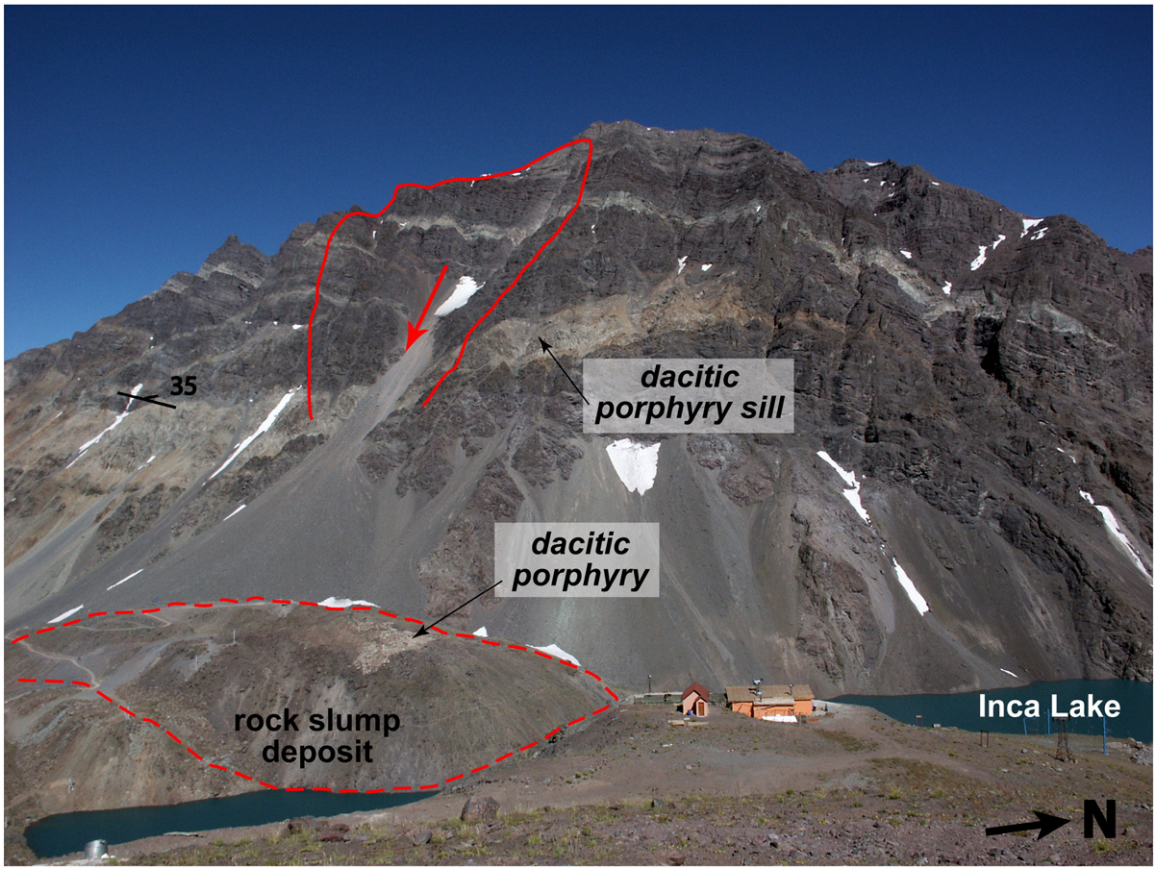

Fig. 4. West lobe rockslide deposit below west valley wall (see S2 in Fig. 5). The white dacitic porphyry stratigraphically entrained in this deposit is only found in the dacitic porphyry sill in the west wall.

as a surface of the body of which it is part, and gives a means of measuring the length of time of exposure (Gosse and Phillips, 2001). Elevation, snow and vegetation cover, and geometric shielding from nearby obstructions are site-specific conditions known to affect production rates (Dunne et al., 1999). Among the systematic errors associated with the method, the most common are a poorly known exposure history, significant erosion of the exposed surface, and invalid assumptions of isotope production rates. A comprehensive review of TCN dating is provided by Gosse and Phillips (2001). Depending on the surface preservation and exposure history, the dating technique has an effective range from the Pliocene (2.65 Ma) to the late Holocene (<10 ka). The advantage of this analytical method is that only the rockslide material is required for dating and that an exact date is provided assuming the rockslide event was instantaneous (Ballantyne et al., 1998). TCN dating has been previously used for separating complex rock avalanche deposits of several generations into various events (Hermanns et al., 2001, 2004).

A total of 17 samples were taken from the various lobes in the study area and from the east wall sliding surface for cosmogenic nuclide dating by ^{36}Cl (see Fig. 5 sampling locations). The samples were collected following the guidelines recommended by Gosse and Phillips (2001), recording the rationale for sample selection, description of rock block sampled, geologic description of sample, location, orientation, sample thickness, and shielding geometry. Nine samples were prepared and concentrated at the PRIME Lab at Purdue University. The ages derived were calculated using the program CHLOE developed by Phillips and Plummer (1996).

Results from the dating are presented in Table 1. These show two different ages, independent of the range of erosion rates assumed for hard volcanic rocks based on a similar work done by Costa and Gonzalez-Diaz (2007) in the Argentinian Patagonia (typically 0.5–2 mm/ka). All ages point towards a post-glacial origin for the deposits and the occurrence of at least two separate sets of prehistoric rockslide events in the Portillo valley. The older deposit corresponds to the Portillo Rock Avalanche event and is dated at about 13.4 ka. A separate deposit south of this, at sampling location P05–01 in Fig. 5, yields similar ^{36}Cl values suggesting that it was simultaneous with the PRA event. The inferred initiation zone for this deposit is the southern rock slope above it. The younger event(s) is dated to 4.4 ka and is associated with the S1 and S2 deposits at the bottom of the east and west slopes (S1 and S2 in Fig. 5, respectively). Considering the significant reworking of the deposits that has occurred as part of the operations of the ski resort, it is difficult to establish whether the 4.4 ka event(s) derives entirely from the Caracoles Range along the east side of the valley or from the west side of the valley as well. This is discussed in more detail below.

2.4. Reconstruction of rockslide failure scenarios

Of the two sets of dated rockslide deposits, the Portillo Rock Avalanche deposit (labelled PRA and H in Fig. 5) is the only one that has a common and characteristic lithology and well-defined source area. Its sliding surface is largely planar, rising up to a peak of 4050 m. a.s.l. with a vertical relief of *ca.* 1000 m (Fig. 6). Given the prehistoric nature of the slide, the exact failure geometry and failure mechanism are unknown. Fig. 7 presents a schematic reconstruction of the failure geometry based on mapping data collected during the field investigation. The proposed failure mechanism involves planar sliding along bedding accommodated through shearing of tectonically disturbed, weaker rock at the toe of the slope. The key constraints for this projection of the pre-failure topography were the mapped location of the thrust fault, the hypothesized dip-slope failure mechanism and the estimated thickness of the slab, as described below.

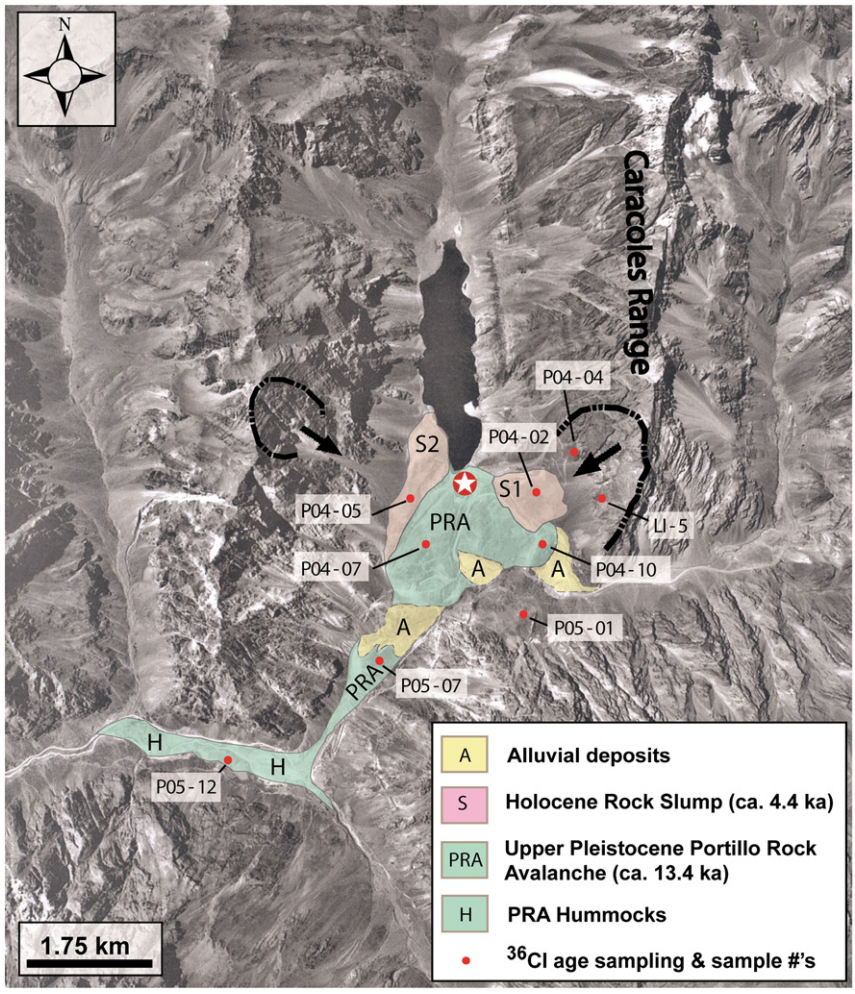

Fig. 5. Aerial photograph (1:80,000) showing the distribution of rockslide deposits, their respective scarps and approximate ages. The star indicates the location of the Portillo Ski Resort.

The cross-section of the pre-failure topography (Fig. 7) was constructed to account for the concave shape observable in the present-day slopes along the Caracoles Range. Terrestrial laser scanning measurements (LiDAR), as described later in Section 4, were used to constrain the dips of the bedding planes as gradually varying from 65°W in the upper part of the slope to 50°W in the lower slope. The thickness of the failed slab was calculated based on estimates of the volume of the slide debris and surface area of the exposed scarp (Fig. 6). Volume estimates for the Portillo Rock Avalanche were based on the empirical correlation proposed by Li (1983), which relates the logarithm of the aerial exposure (A) of the deposit in m^2 with the logarithm of the volume (V) in m^3:

$$\mathrm{Log}(A) = 1.9 + 0.57 * \mathrm{Log}(V). \quad (1)$$

This returns a calculated volume of the debris for the Portillo Rock Avalanche deposit of 68 million m^3. Assuming a volume increase of 25% due to fragmentation of the detached mass during transport (Hungr and Evans, 2004), and assuming minimal entrainment, this would give a pre-failure (in place) volume of the rockslide of approximately 50 million m^3 and an estimated depth of failure of 65 m ± 10 m. Because the trace of the thrust fault is covered by talus immediately below the scarp of the Portillo Rock Avalanche, the corresponding uncertainty in its exact location results in a ±10% difference in the failure depth estimated.

As with the reconstruction of the pre-failure slope geometry, the prehistoric nature of the failure only allows speculation with regard to the rockslide triggering mechanism. Based on the steepness of the bedding/slope, one that exceeds the frictional strength along the bedding planes, kinematic release may have been triggered by a large earthquake, perhaps aided in part by oversteepening of the valley walls and debuttressing of the slope after the last glacial maximum (i.e. approximately 14.5 ka). This age would agree with that obtained for the Portillo Rock Avalanche deposits through the cosmogenic nuclide dating. A progressive strength degradation mechanism (see Eberhardt et al. (2004)) may also have contributed to failure, in the form of both asperity breakdown along the bedding planes and loss of coherence in the stronger units at the toe of the slope over time.

The remaining rockslide deposits (S1 and S2 in Fig. 5), were initially interpreted and mapped as lateral moraines due to their distinctive morphology (Caviedes and Paskoff, 1975), but this interpretation was discounted once the cosmogenic nuclide dating was performed and indicated that the sampled lobes were post-glacial in age (4.4 ka). These results were also supported by detailed inspection of the deposits. As previously noted, significant reworking of these deposits and the surrounding terrain through operations related to the ski resort makes it difficult to establish whether the two younger deposits (S1 and S2) are derived from a single event originating from the eastern Caracoles Range and travelling across the valley, or correspond to two simultaneous events derived from the east (S1 deposit) and west sides of the valley (S2 deposit), perhaps triggered by an earthquake given their temporal and spatial proximity.

In the case of the first hypothesis, the leading edge of the rockslide would have had to travel approximately 2 km westward across the

Table 1
Mapping data and ages obtained through ^{36}Cl cosmogenic nuclide dating, reported to one standard deviation. Note that longitude and latitude are based on Datum WGS 84.

	P0402	P0404	P0405	P0407	P0410	P0501	P0507	P0512	LI-5
Rock type	Andesite	Andesitic tuff	Andesitic tuff	Andesitic tuff	Andesitic porphyry	Pyroxene-rich andesite	Andesitic tuff	Andesite	Andesitic tuff
Longitude (W)	70.1	70.1	70.1	70.1	70.1	70.1	70.1	70.2	70.1
Latitude (S)	32.8	32.8	32.8	32.9	32.9	32.8	32.9	32.9	32.8
Elevation [m]	2990	3120	2952	3049	2953	2909	2574	2215	3200
Block geometry – $L\times W\times H$ [m]	2.5×1×1.2	Slide scarp	1×0.5×0.5	5×4×2	4×3×2.5	3×4×2	5×4×2	2.5×2×1.5	0.25×0.13×0.03
Orientation of sample surface [°]	0	40	36	5	20	0	0	18	55
Maximum angle of shielding geometry [°]	33	40	34	25	30	40	40	44	40
Calculated age [ka] assuming erosion rate of 0.56 mm/ka	4.1 ± 0.3	12.7 ± 1.0	4.2 ± 0.5	14.9 ± 1.7	12.1 ± 0.5	14.5 ± 1.2	14.2 ± 1.0	13.6 ± 0.6	5.0 ± 0.4
Calculated age [ka] assuming erosion rate of 2.22 mm/ka	4.1 ± 0.3	12.3 ± 1.0	4.1 ± 0.5	14.4 ± 1.6	11.5 ± 0.5	13.9 ± 1.1	13.2 ± 0.9	12.9 ± 0.5	4.9 ± 0.3

valley overriding the previously deposited Portillo Rock Avalanche debris, run up the base of the west slope and land at its toe as it fell back forming a fall-back ridge. The lack of continuity between the eastern and western deposits could then be explained by the reworking of the terrain for the development of the ski resort. For the second hypothesis, the source of the lobate deposit found at the foot of the western slope could be explained as originating from a rock slump/collapse from the west wall whose short runout could be attributed to unfavourable geometrical conditions for motion created by the dip of the beds on that side of the valley into the slope. The deposits at the foot of the eastern slope would then have occurred through a simultaneous event originating from the steep Caracoles Range slope on the east side of the valley. Comparing the arguments supporting each hypothesis, it was decided that the most likely scenario was that of simultaneous events from two different source areas. This scenario was later supported by the dynamic runout analyses performed, which are presented in Section 5.2.

3. Methodology and hazard assessment procedure

To assess the hazard level posed to the International Santiago–Mendoza Corridor and ski resort at Portillo, back analyses and forward modelling were carried out linking failure initiation to rockslide runout following the framework developed by Strouth and Eberhardt (2009). The methodology begins with using geological and geotechnical mapping data to help develop and provide input for numerical models directed at back analyses of a representative rock slope failure in the area. Here, the distinct-element code UDEC (Itasca, 2004) was used to back analyze the Portillo Rock Avalanche and assess the likely failure mechanism. Understanding derived from these models, such as deformation characteristics, kinematics prior to failure and projected rockslide volume, was then used to aid in the modelling of 3-D post-failure movement and dynamics using the dynamic/rheological flow code DAN3D (McDougall and Hungr, 2004). Insights gained from both sets of these back analyses were then applied to forward modelling of potential instability of the current slope and travel path and velocities of a rockslide runout in the event of failure. Thus, this framework links the properties, kinematics and mechanisms important to understanding both failure initiation and runout.

Following this framework, several objectives were targeted by the analyses. With respect to the failure mechanism of the Portillo Rock Avalanche, assessing the importance of the primary discontinuity sets (i.e. internal structure of the slide mass) and rock mass properties in relation to the failure kinematics and nature of the toe-release of the slide mass was deemed a key objective given the non-daylighting nature (i.e. slope-parallel dip) of the volcaniclastic bedding. With respect to the runout simulations, constraining and characterizing the travel path and rheological behaviour of the Portillo Rock Avalanche together with those of the other prehistoric rockslides mapped at the study site (i.e. the Holocene S1 and S2 slides in Fig. 5) were key objectives. The objectives of the forward modelling then followed as including the stability analysis of the present-day rock slope at Portillo along the Caracoles Range, testing its sensitivity to various triggering mechanisms including an elevated water table and seismic shaking (i.e. earthquake trigger), and determining the extent and reach of the rockslide debris in event of another (worst case scenario) rock avalanche.

3.1. Dip-slope failure mechanisms and numerical analysis

A significant amount of work has been published on the failure initiation of large rock slopes. In massive rock slopes where adverse dipping discontinuities are not fully persistent, failure may occur through a combination of sliding along discrete planes and internal shearing of the rock mass (Eberhardt et al., 2004). For dip slopes, where sliding may be promoted by slope-parallel persistent planes of

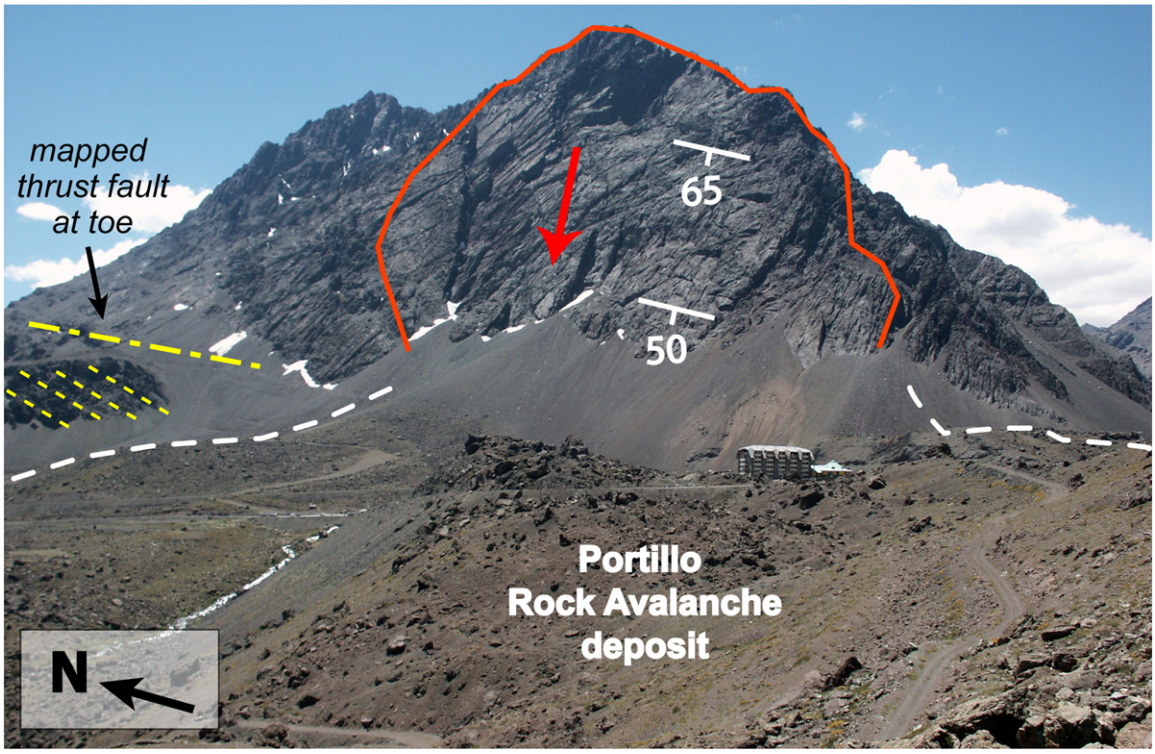

Fig. 6. East slope along Caracoles Range and source area of the Portillo Rock Avalanche deposit. Also shown is the thrust fault mapped at the toe of the slope and the back dipping bedding below it (see Fig. 7).

weakness (e.g. bedding), the absence of a daylighting structure dipping out of the slope requires that failure develops through a bi-planar or step-path failure mode accommodated through shearing at the toe, otherwise referred to as toe breakout (Fisher and Eberhardt, 2007). The failure mechanism for these slopes is therefore guided by a damage or transition zone between the active upper slope and the passive toe (Mencl, 1966; Kvapil and Clews, 1979; Fisher and Eberhardt, 2007). Kvapil and Clews (1979) describe this transition zone as coinciding with a change in direction of the acting stresses and intense fracturing of the rock.

The key role internal shearing and toe break out play in the dip-slope failure mechanism limits the applicability of limit equilibrium analyses. Instead, several authors (Coggan et al., 1998; Kimber et al., 1998; Eberhardt et al., 2004; Stead et al., 2006) recommend the use of numerical modelling techniques (continuum and discontinuum) as a more effective tool where internal slope deformation and complex failure mechanisms are involved. For the Portillo investigation, a discontinuum approach was adopted using the commercial distinct-element code UDEC (Itasca, 2004). This approach is ideal for modelling failures in natural jointed systems, where the problem domain corresponds to an array of distinct, interacting blocks that can be subjected to external loads, large strain displacements and block rotations (Stead et al., 2006; Strouth and Eberhardt, 2009).

To constrain the failure initiation models developed and presented here, the field investigation program was planned to target specific data sets required for discontinuum modelling. This included data required to represent the discontinuity network, especially persistence and spacing, and the determination of discontinuity and rock mass properties. These are described in detail in Section 4.

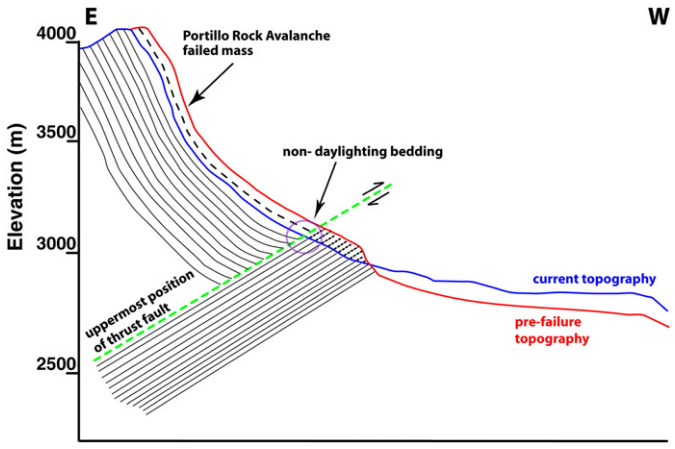

Fig. 7. Cross-section through east slope showing reconstructed pre-failure topography and rockslide geology.

3.2. Triggering factors

The two most common trigger mechanisms for large rockslides are heavy precipitation, which can induce changes in effective stress that may overcome the material strength due to build up of pore-water pressures, and earthquakes which may cause a slope failure due to the extra load induced by ground shaking during the event. When a rock slope is affected by dynamic loading, the material strength, slope geometry, pore-water pressure, and number of cycles of the ground motion (or duration of the event) are the key factors which will determine if a rockslide is triggered (Keefer, 1984). The depth of the earthquake and distance of the source from the slope in question are also important constraints.

For the failure initiation analyses carried out, the effects of groundwater and the sensitivity of the models to a precipitation trigger were tested using UDEC's coupled hydro-mechanical steady-state flow algorithm (Itasca, 2004). The formulation limits fluid flow to the discontinuity network (i.e. the blocks bounded by the discontinuities are assumed to be impermeable), with flow being controlled by the joint aperture based on the cubic law (for fluid flow between two parallel plates; see Priest (1993)). The hydro-mechanical coupling thus relates mechanical deformation occurring in the form of normal joint displacements to joint

aperture (i.e. joint closure or opening), which in turn changes the joint hydraulic conductivity and the subsequent distribution of joint water pressures; conversely, changing joint water pressures result in a corresponding change in mechanical aperture, as well as in the effective stresses acting along a joint thereby creating the potential for slip (Olsson and Barton, 2001).

Testing of model sensitivity to an earthquake trigger was performed using the dynamic loading algorithm in UDEC (Itasca, 2004). The formulation works to solve the equations of motion, including the inertial terms, using the real mass of the blocks rather than scaled inertial masses as in a static solution. This means that the generation and dissipation of kinetic energy is directly affected by the solution. The key inputs required to construct the dynamic models used here were the definition of the dynamic loading and boundary conditions, mechanical damping, and wave transmission through the model. Wave propagation and interactions (e.g. reflection) at the model boundaries are reduced by setting either quiet or free-field boundary conditions (Itasca, 2004). Mechanical damping is applied to account for energy losses due to internal friction in the intact material and slip along the discontinuities (Itasca, 2004; Wyllie and Mah, 2004). Raleigh damping was used in this study as it provides damping that is approximately frequency independent, similar to the hysteretic behaviour of natural damping (Itasca, 2004). The dynamic input was applied assuming a velocity history represented by a harmonic sine function. The determination and definition of this velocity record is described in more detail with the presentation of the analysis results.

3.3. Runout prediction of failed slopes

Runout analyses, within the framework of quantitative landslide risk assessment, provide a means to constrain the travel path, reach, velocities and intensity of long runout rockslides (Hungr et al., 2005). Analyses may be empirical, using historical data like volume, fall height, distance travelled, etc. (e.g. Scheidegger, 1973; Corominas, 1996), and/or numerical, based on solid and fluid dynamics with an aim to model moving landslides and their complex behaviour passing from sliding to flowing (Hungr et al., 2005).

A numerical approach was taken for this study using the dynamic/rheological flow code DAN3D (McDougall and Hungr, 2004). DAN3D is based on a Lagrangian Smoothed Particle Hydrodynamics (SPH) formulation, which enables the modelling of complex, multi-directional rockslide movement over equally complex 3-D terrain. The code accounts for specific features of the rockslide being analyzed such as internal strength, material entrainment and rheology variations. McDougall et al. (2008) have shown through back analyses of a number of case histories the ability of such codes to consistently simulate actual events. Thus with proper calibration of the input parameters, the model has the ability to provide first-order predictions of landslide flow behaviour, including direction, velocity, depth and runout extent. Key input required for a DAN3D analysis includes a digital terrain model (DTM) of the runout path, the volume and initial location of the sliding mass, an appropriate rheological model, and constitutive properties of the runout material and runout path. These were estimated and calibrated using runout characteristics mapped in the field together with results obtained from the numerical modelling of failure initiation, as discussed later in Section 5 of the paper.

4. Geotechnical characterization of the east slope

4.1. Discontinuity network

A key to understanding the kinematics of the Portillo Rock Avalanche failure was the data regarding the dominant large-scale structures and persistent discontinuities. Scanline mapping was

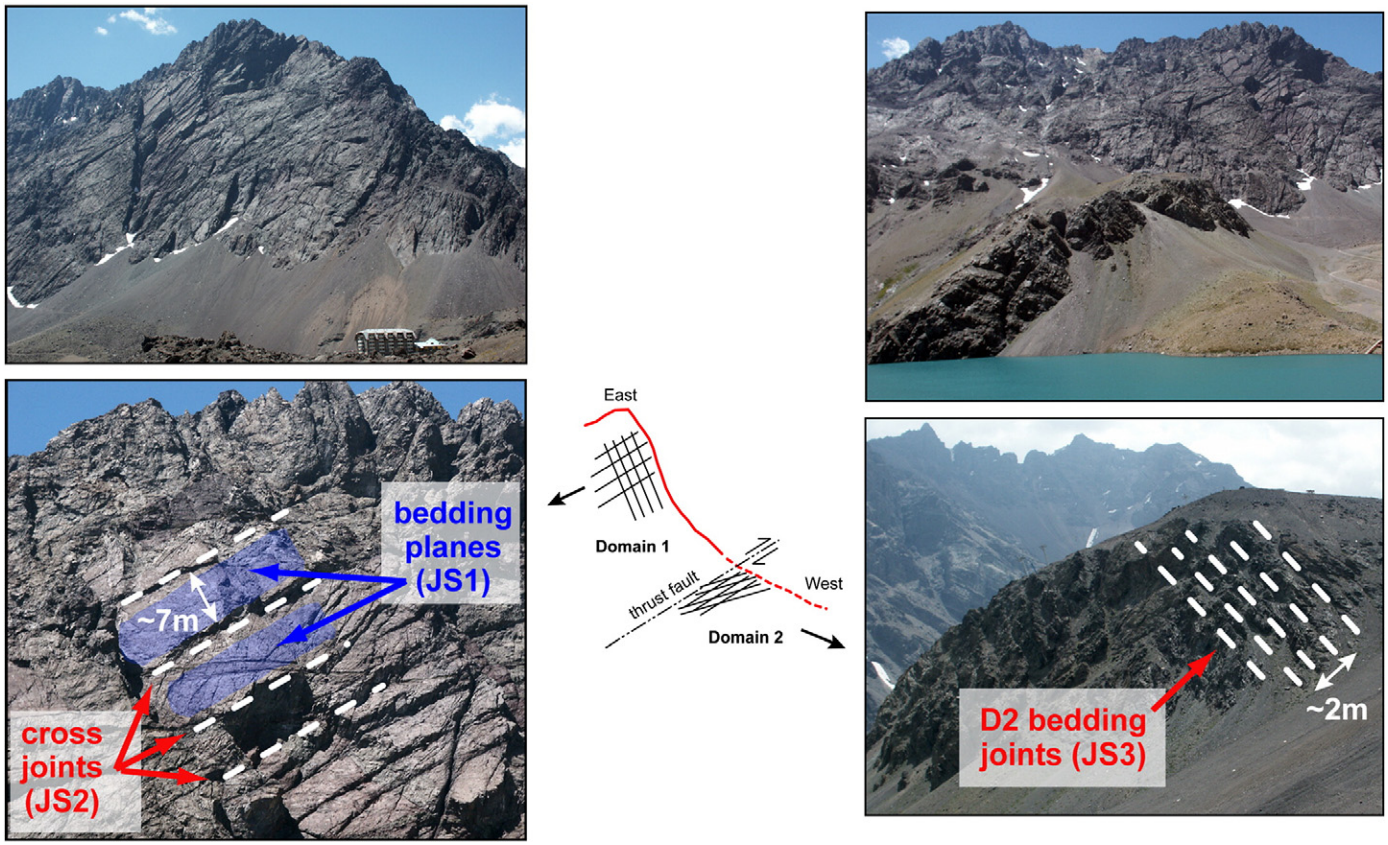

Fig. 8. Profile of the eastern slope showing the locations of structural domains D1 and D2 relative to the thrust fault mapped in the slope, and photos illustrating the key joint sets and their relative spacing.

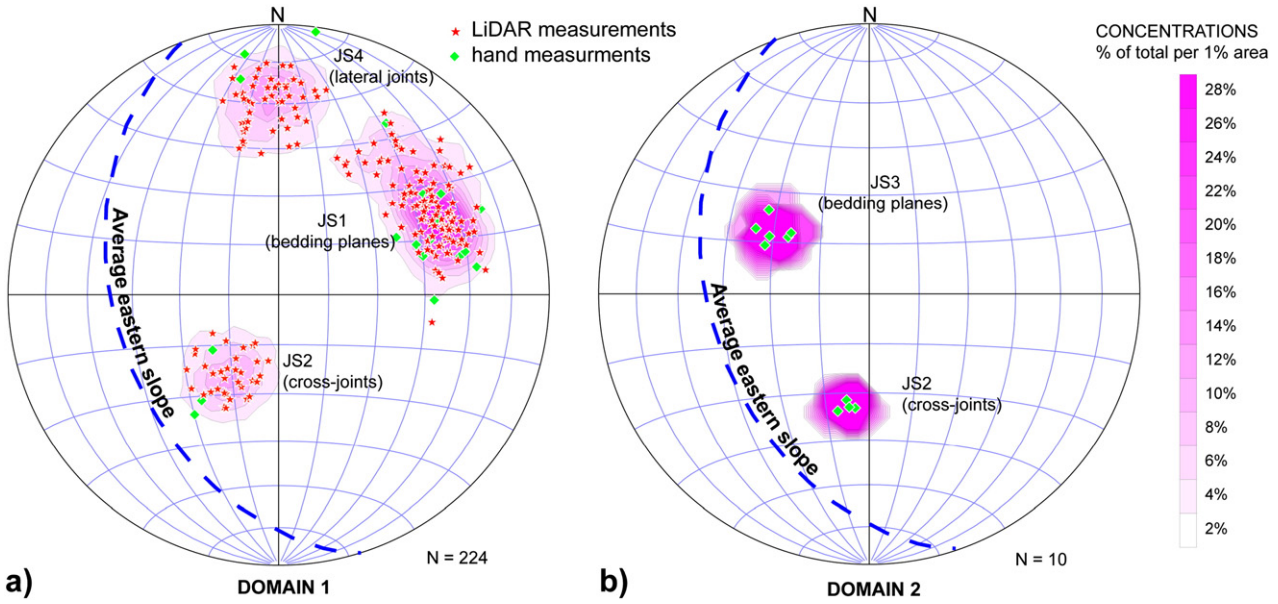

Fig. 9. Equal area (Schmidt) lower hemisphere stereonet pole projections of hand and LiDAR joint measurements for: a) Domain 1; and b) Domain 2. Superimposed is the great circle trace of the average orientation and dip of the eastern slope face.

carried out along the base of the eastern slope to characterize these features. These measurements were complimented with those from a detailed 3-D terrestrial laser scanning (LiDAR) survey, carried out to digitally map the upper sections of the slope due to restrictions in accessibility posed by the steepness of the slope and rockfall hazard from above. An Optech ILRIS-3D laser scanner was used.

Based on the mapping and LiDAR results, the slope was divided into two distinct structural domains differentiated by the degree of rock mass damage related to the presence of the thrust fault. Domain 1 (D1) corresponds to the hanging wall of the thrust fault and includes the upper slope. Domain 2 (D2) corresponds with the footwall and includes the zone of heavily damaged rock (Fig. 8). In D1, two dominant discontinuity sets were recognized (Fig. 9a): a persistent bedding plane (JS1) and a cross-cutting joint set (JS2). Also present is a persistent, although less frequent, set of lateral release joints JS4. It is believed that the generation of JS2 is syntectonic to the generation of the thrust fault mapped at the toe of the eastern slope, which explains its continuity into D2 (Fig. 9b). In the highly fractured D2, the bedding dips into the slope as opposed to parallel to the slope, as in D1, and therefore was differentiated as JS3 (Fig. 9b). The bedding planes in D1 were assumed to be fully persistent based on their geological origin, namely stratification in the volcaniclastic rocks, and together with the cross-jointing were widely spaced forming large tabular blocks (Fig. 8). Inspection of the LiDAR data suggested that the JS1 bedding was smooth, with scatter in the azimuth measurements being interpreted as a large-amplitude undulation (Fig. 9a). The JS2 joints were found to have rougher surfaces with less undulation. In D2, the JS2 and JS3 joint sets were mapped as having a high persistence and close spacing (<2 m; Fig. 8). In this domain the more intense fracturing is clearly a representation of the rock damage produced during the development of the thrust fault. Coherence between the LiDAR and scanline hand measurements lent confidence to the assessed values.

4.2. Rock mass properties

Rock mass properties were determined through a combination of laboratory testing and rock mass characterization. Laboratory testing involved uniaxial and triaxial compression tests, following ASTM standards. The intact rock properties of the main geologic units (andesite, andesitic tuff) derived from these tests are summarized in Table 2. Mated samples were also retrieved from a bedding plane surface in Domain 1 (JS1) for which direct shear tests were carried out, following ASTM standards, in the direction of sliding. Average joint friction angles of 49° peak and 45° residual were obtained. However, given the non-representative scale of the laboratory samples relative to the rock slope itself, the test results were only used to guide estimates of the rock mass and discontinuity properties required for the numerical modelling.

The rock mass characteristics were assessed in the field using the Geological Strength Index, GSI (Hoek et al., 1995; Marinos et al., 2005), and Bieniawski's (1989) Rock Mass Rating (RMR_{89}). GSI values were evaluated as a range of values rather than as a single value for each domain. The RMR value determined for each domain was based on the modified RMR^*_{89}, as per Hoek et al. (1995), in which the groundwater rating was set to 'dry' conditions and the penalty for joint orientation was set to zero. These adjustments avoid double counting the effects of groundwater and joint orientation when deriving rock mass properties to be used in numerical analyses where the influence of groundwater and adverse jointing are explicitly accounted for. Table 3 shows the GSI and RMR^*_{89} values mapped in the field for Domains 1 and 2. These range from blocky to very blocky conditions for D1, with discontinuities having good to fair surface

Table 2
Average intact rock strength values obtained from uniaxial and triaxial laboratory testing.

Rock unit	Density [kg/m^3]	Young's modulus [GPa]	Poisson's ratio [–]	Uniaxial compressive strength [MPa]	Intact cohesion [MPa]	Intact friction angle [°]
Andesite	2650	42.3	0.18	97.3	–	–
Andesitic tuff	2650	48.9	0.25	250.0	56	49

Table 3
GSI and RMR^*_{89} values mapped in the field for Domains 1 and 2.

	Domain 1	Domain 2
GSI	70–50 Blocky to very blocky	50–35 Very blocky to disturbed
RMR^*_{89}	82–67 Good to very good	56–44 Fair
GSI_{RMR89}[a]	77–62	51–39

[a] Equivalent GSI obtained from relationship: $GSI = RMR^*_{89} - 5$ (Hoek et al., 1995).

Table 4
Range of lab and field-based input parameters, and calculated Hoek–Brown (H–B) and Mohr–Coulomb (M–C) rock mass properties for Domains 1 and 2.

Input:	Intact rock properties	Units	Domain 1	Domain 2
	Uniaxial compressive strength	[MPa]	90–250	30–60
	Geological Strength Index	[–]	50–70	35–50
	H–B constant, m_i	[–]	11.3	11.3
	Young's modulus, E_i	[GPa]	40–55	9–30
	Poisson's ratio, ν	[–]	0.2–0.3	0.2–0.3
	Density, ρ	[kg/m^3]	2700	2600
Output:	Rock Mass Properties			
	H–B constant, m_b	[–]	2–4	0.9–1.8
	H–B constant, s	[–]	0.004–0.04	0.0007–0.004
	H–B constant, a	[–]	0.5	0.5
	M–C cohesion, c	[MPa]	4–10	2–4
	M–C friction angle, ϕ	[°]	33–46	20–30
	Tensile strength, T_0	[MPa]	33–46	20–30
	Deformation modulus, E_{rm}	[GPa]	12–40	1–9

conditions, to very blocky to disturbed conditions for D2, with discontinuity surface conditions varying from poor to fair.

Rock mass properties for Domains 1 and 2 were next estimated using the empirical scaling relationships developed by Hoek et al. (2002). Although the distinct-element method allows for the explicit inclusion of mapped discontinuities, a 1:1 representation is usually not practical due to the excessive computing run times that would result. Instead, a balance is struck between a larger joint spacing that still permits the key kinematic influence of the joint network to be captured and the use of equivalent continuum rock mass properties for the intact blocks that account for the strength weakening effect of the full fracture network. Table 4 reports the resulting Hoek–Brown rock mass properties for Domains 1 and 2 together with the extrapolated Mohr–Coulomb rock mass properties. It should be noted here that the quantitative conversion of Hoek–Brown to Mohr–Coulomb parameters is done by fitting an average linear Mohr–Coulomb relationship to the non-linear Hoek–Brown envelope for a range of minor principal stress values defined by the upper limit of confining stress σ_{3max} for the problem (Hoek et al., 2002). This was based here on the slope height of the Portillo Rock Avalanche. Table 5 reports the discontinuity properties estimated for Domains 1 and 2. These were based on results from the direct shear tests, field-based observations, values published by Kulhawy (1975) for volcaniclastic rocks, and those calculated using the relationships published by Barton (1972).

4.3. Hydrogeology

Mapping of the hydrogeological conditions at the site revealed little to no indications of water seeping from the face of the Portillo Rock Avalanche source area. Similarly, the slope contains no vegetation that would suggest the presence of water. Based on this information it is inferred that the slope is mostly dry with the water level near the toe of the slope coinciding with Inca Lake (2800 m.a.s.l.). Wyllie and Mah (2004) note that sometimes the seepage rate is lower than the evaporation rate resulting in a slope that is dry in appearance, but that significant pore-water pressures may still be present within the rock mass at depth. Assuming that groundwater flow for the eastern slope is controlled by fracture permeability, the discontinuity network derived for this study, although simplified, suggests that flow would be parallel to bedding in the upper parts of the slope until it reaches the flow barrier created by the fault at the toe of the slope. Here pore-water pressures and flow may dissipate through the more heavily fractured rock mass.

Table 5
Estimated range of discontinuity strength and stiffness parameters for Domains 1 and 2.

Discontinuity property	Units	Domain 1	Domain 2
Joint friction angle, ϕ_j	[°]	30–50	20–30
Joint cohesion, c_j	[MPa]	0–1	0–0.05
Joint normal stiffness, jkn	[GPa/m]	3–25	1–12
Joint shear stiffness, jks	[GPa/m]	1–10	0.5–6

5. Back analysis of the prehistoric Portillo Rock Avalanche event

5.1. Failure initiation

Initial assessments based on visual observations suggest that failure occurred primarily along slope-parallel bedding planes in a translational manner. However, mapping of the source area (i.e. the eastern slope) revealed no daylighting of persistent structures to explain a simple kinematic release mechanism. Given that the steepness of the bedding/slope (50–65°) exceeds the frictional strength along the bedding planes (the upper limit of which was determined to be 50°), kinematic release is assumed to have occurred through yielding of the weaker fault material at the toe of the slope due to the loading imposed by the upper slope. Distinct-element modelling was carried out to confirm this failure mechanism and to test its sensitivity to varying geometry assumptions and shear strength properties.

Fig. 10 depicts the model geometry used. Given that movement of the Portillo Rock Avalanche is assumed to have occurred in the direction of steepest dip (parallel to bedding), the 2-D plane strain assumption adopted was deemed to be reasonable. Both Domains 1 and 2 were represented in the model, with the key controlling discontinuities being explicitly represented using the orientations obtained from outcrop and LiDAR mapping. Joint spacings were scaled for computational efficiency maintaining the average JS1:JS2 spacing ratio of 3:4 (Fig. 10). The source volume and surrounding rock mass were treated as a discontinuous, Mohr–Coulomb elasto-plastic material. The material properties were taken from those reported in Tables 4 and 5. Values were varied within the ranges specified, with those closer to the lower bound strengths best reproducing the estimated failure volume. The in situ stresses were initialized assuming a horizontal to vertical stress ratio of 2 (i.e. compressive regime), based on the regional stress tensor for the central Andes determined using earthquake focal mechanisms by Pardo et al. (2002) and Barrientos et al. (2004). The back analyses were performed without considering pore-water pressures given the uncertainty of the prehistoric conditions and the general absence of springs or seeps at the toe of the slope (pore pressures are later included for the forward analyses). Moreover, a sensitivity analysis was performed with respect to joint friction, which implicitly would have included the influence of water in reducing the effective stresses on the failure mechanism modelled.

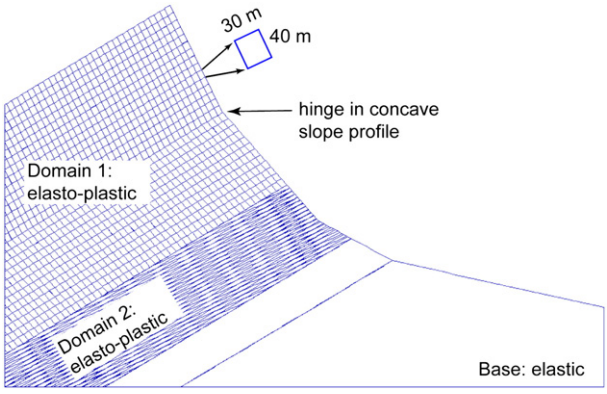

Fig. 10. UDEC model geometry used to model failure initiation of the prehistoric Portillo Rock Avalanche event.

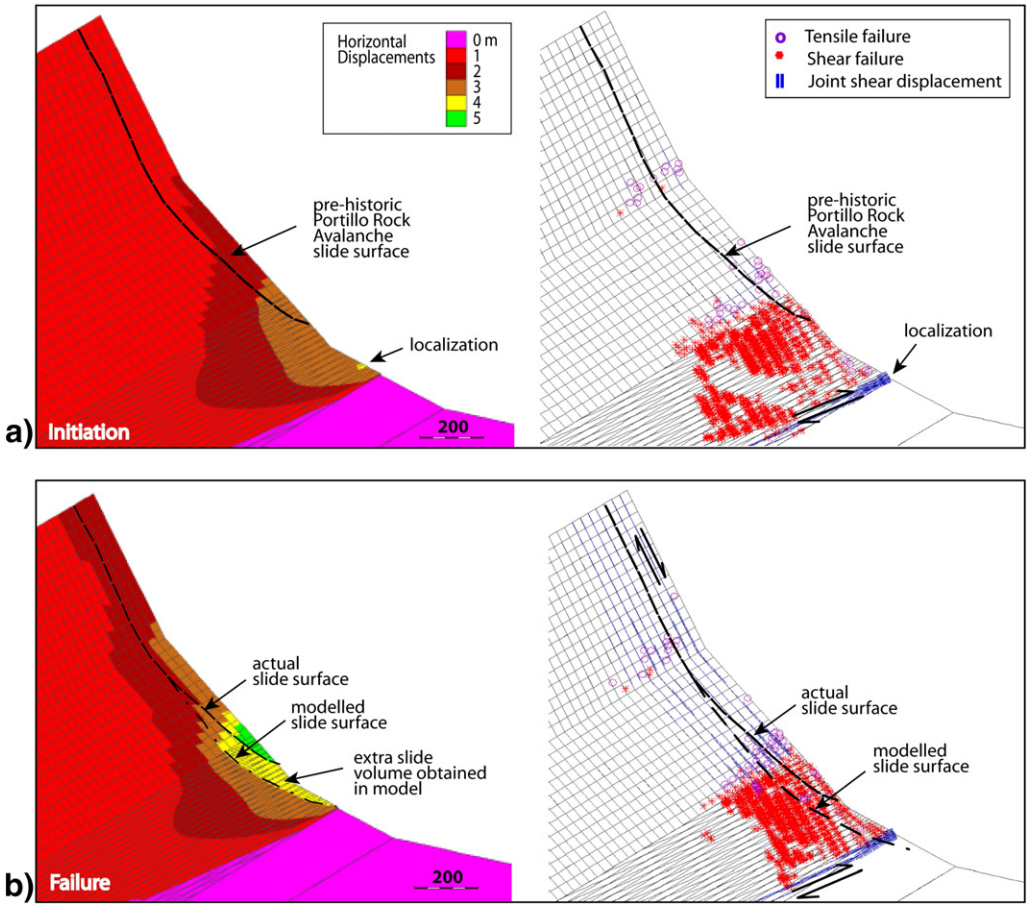

Fig. 11. Evolution of horizontal displacements and plasticity indicators from a) localization and initiation, to b) failure. Superimposed are the mapped failure surface of the prehistoric Portillo Rock Avalanche event and that interpreted in the UDEC models.

A staged analysis was performed to simulate progressive strength degradation through incremental lowering of the rock mass cohesion to simulate the loss of coherence in the stronger units at the toe of the slope through brittle fracture processes, while joint cohesion was reduced to represent the destruction of asperities and intact rock bridges between non-persistent joints. Fig. 11a shows failure initiation using this procedure when the rock mass cohesion drops from 10 to 6 MPa and joint cohesion is reduced from 1 to 0.01 MPa. The amount of horizontal displacement increases to magnitudes suggesting catastrophic failure when the rock mass and joint cohesion are further reduced to 2 and 0 MPa respectively (Fig. 11b).

Based on the plasticity, shear, displacement, and velocity indicators, the predicted rupture surface extends deeper into the slope in Domain 2 compared to the mapped surface, therefore adding extra volume (approximately 20% or about 12 million m^3). Testing a number of model and parameter variations, the best fit in terms of estimated volume and mapped failure surface was achieved when Domain 2 was represented as an elasto-plastic continuum as opposed to an elasto-plastic discontinuum (Fig. 12). Otherwise, the failure mechanism reproduced

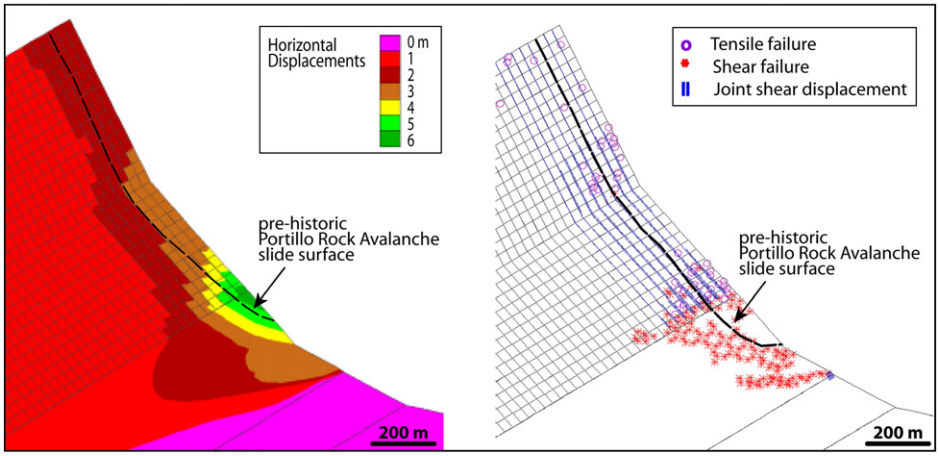

Fig. 12. Horizontal displacements and plasticity indicators for modelled failed state where Domain 2 is modelled as an equivalent continuum. Superimposed is the mapped failure surface of the prehistoric Portillo Rock Avalanche event.

was always the same independent of the strength parameters, geometry and constitutive models tested. This consistency in the model results provided a high degree of confidence with respect to model and parameter uncertainty related to the prehistoric rockslide.

Shear displacements and plasticity indicators show a mechanism that involves failure initiation at the toe through brittle fracture processes and rock mass yielding. This shearing is concentrated at the base of Domain 2, augmented by the active driving compressive forces exerted by the upper slope (Domain 1) parallel to bedding. Tensile failure above Domain 2 suggests a staged failure, controlled in part by a "Prandtl"-like wedge (see Kvapil and Clews (1979)) between the active and passive zones. Upwards propagation of the tensile damage and brittle fracturing (Fig. 11b), aided by the cross-cutting joints, then enables kinematic release at the toe, which in the absence of a cross-cutting daylighting discontinuity dipping out of the slope would otherwise not be kinematically possible. The failure of the lower portion of the slope, which provides support for the upper slope, subsequently enables translational kinematic release of the upper slope along bedding up to the slope crest. Thus, this failure mode is accommodated and highly controlled by the adverse geometry of the slope and bedding.

5.2. Runout analysis

Dynamic runout analyses were carried out using the numerical code DAN3D (McDougall and Hungr, 2004). This continuum dynamic model is governed by internal and basal rheological relationships. The internal rheology is assumed to be frictional and is ruled by the internal friction angle (ϕ). The basal rheology was selected based on the characteristics of the slide and valley fill materials along the slide paths. These included:

Frictional:

$$\tau_{zx} = -\sigma_z(1-r_u)\tan\phi \tag{2}$$

Voellmy:

$$\tau_{zx} = -\left(\sigma_z f + \frac{\rho g v_x^2}{\xi}\right) \tag{3}$$

where τ_{zx} is the basal shear stress opposing motion, σ_z is the total normal stress at the base of the slide, r_u is the pore pressure ratio, ϕ is the dynamic basal friction angle, f is the frictional coefficient (analogous to $\tan\phi_b$, where ϕ_b is the bulk basal friction angle), ρ is the material density, v is the depth-averaged flow velocity, and ξ is the turbulence term.

The frictional relationship in Eq. (2) shows that the shear strength represented by frictional basal resistance is proportional to the effective bed-normal stress at the base. The relationship can be further simplified to requiring one-independent variable by replacing the dynamic basal friction angle (ϕ) by a bulk basal friction angle (ϕ_b) with constant pore pressure ratio (r_u). In this case, the loading response of the overridden material lies between purely drained, where little entrainment is expected, and undrained, where failure and mobilization of the bed material are expected due to excess pore-water pressures (McDougall, 2006). Because r_u is kept constant, Eq. (2) still has a frictional character even though it represents material friction and pore-fluid pressures (Hungr et al., 2005).

The Voellmy rheology is a two-parameter frictional–turbulent resistance relationship. The first component in Eq. (3) is the frictional term and is equivalent to Eq. (2), where $\phi = \tan\phi_b$. The second component accounts implicitly for all possible sources of velocity-dependent resistance (McDougall, 2006). As a result, the use of a Voellmy basal rheology in landslide simulations predicts lower maximum velocities for a given overall displacement compared to a constant frictional rheology and more uniform distribution of debris in the deposition area (Hungr et al., 2005).

Combinations of these two basal rheologies were tested and ranked based on their ability to reproduce the mapped distribution of rockslide deposits, and further tested against temporal constraints corresponding with the sequence of events established by cosmogenic nuclide dating. In addition to material properties, the key inputs required for the analysis were the pre-failure rockslide volume (estimated from the UDEC modelling) and pre-failure surface topography of the valley (i.e. runout path).

The in-place slide volume of the Portillo Rock Avalanche was estimated to be 50 million m^3 with an average slide thickness of 65 m ± 10 m, as previously discussed. Also required was an estimate of the in-place volume of the Holocene aged rockslide deposit mapped along the western side of the valley (S2 in Fig. 5). This was estimated to involve approximately 16 million m^3 of failed rock, with an estimated average slide thickness of 30 m ± 5 m. The pre-failure topographies were reconstructed using a DTM developed from the current 1:50,000 scale topography map. The calculated volumes of the detached masses were then added to the source areas following the same principles in which the 'Sloping Local Base Level (SLBL)' concept is based (see Jaboyedoff et al., 2004). To reconstruct the prehistoric valley floor (i.e. travel path), the DTM plus a series of E–W and N–S cross-sections constructed perpendicular and parallel to the valley were used to constrain the thickness of the valley floor deposits and depth of Inca Lake. These thicknesses/depths were then subtracted from the present-day valley floor in the DTM, factoring in the glacio-fluvial sediments that would have existed at the time (Fig. 13).

5.2.1. Runout analysis of the Portillo Rock Avalanche event

A combined basal rheology was tested to account for the mobility of the Portillo Rock Avalanche event and superficial valley floor materials encountered. Best fits to the physical characteristics of the rock avalanche deposits were used as a model constraint. The two phases of motion simulated involved using a frictional basal rheology in the proximal path (rockslide source area) and a Voellmy basal rheology in the distal path (valley floor); these are in accord with the probable change in behaviour of the moving mass in terms of response to the shear resistance encountered at the basal interface (see Hungr et al. (2005)). The parameters listed in Table 6 are those that were back analyzed as providing the best fit to the mapped deposits, and correspond with values reported by Hungr and Evans (1996) in their back analyses of 23 rock avalanches. The DAN3D results are presented in Fig. 14. These were seen to provide good agreement with the prehistoric event in several ways. First, the model provides a close match with the general extent and distribution of the deposit, especially with respect to the reach of the leading edge of the debris. Minor differences may be attributed to the omission of small-scale pre-slide terrain features in the reconstruction of the prehistoric path. Of interest are three distinct zones of deposition in the model (Z1, Z2 and Z3 in Fig. 14, $t = 400$ s). These coincide with large mounds evident in the DEM where slope angles in the present-day deposits rise up above 7° from the general down dipping direction of the valley walls. Second, the average simulated deposit depth is approximately 45 m, which falls within the range of the thickness obtained from back-calculating the areal exposure and its associated volume, as well as the range of the thickness estimated in the mapped cross-sections. Third, the runout analysis supports the hypothesis of Inca Lake having been formed by a rockslide dam; a significant amount of the modelled runout material is deposited in front of the south end of where the lake currently ends (Z1 in Fig. 14). The interpretations based on the cosmogenic nuclide dating are also indirectly supported as there is no indication of material being deposited in the area of the S2 lobe (Fig. 5), confirming a different source for the Holocene age-dated deposits located at the foot of the west side of the valley.

5.2.2. Runout analysis of the Holocene rockslide event

The two hypotheses regarding the source(s) of the Holocene rockslide deposits, as previously discussed in Section 2.3, were tested

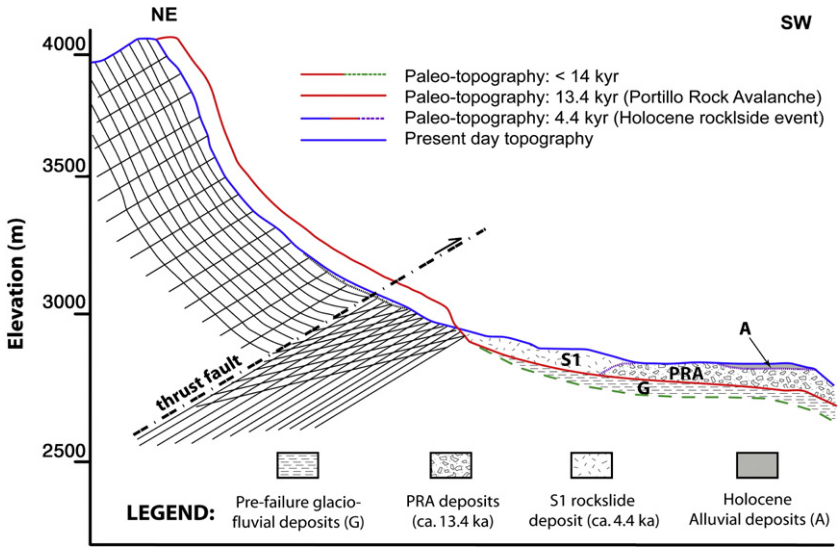

Fig. 13. Cross-section parallel to the runout path followed by the Portillo Rock Avalanche showing the chronology of events and related paleosurfaces.

using DAN3D. For review, these involve scenarios where either both sets of deposits are derived from a single source originating from the east side of the valley, i.e. the Caracoles Range, or that the deposits represent two separate source areas, one originating from the east side of the valley (S1 deposit in Fig. 5) and one from the west (S2 deposit in Fig. 5). The first scenario was quickly discounted as runout simulations for the much larger Portillo Rock Avalanche had already indicated that only a small amount of material, smaller than that mapped for S2, would be deposited at the toe of the western slope following a large volume rockslide originating from the eastern Caracoles Range. Simply, the smaller source volume of the Holocene event does not provide enough momentum to override the higher friction Portillo Rock Avalanche deposits to reach the western side of the valley.

Results for the second scenario are shown in Fig. 15, in which a bulk basal friction angle of 33° was used to represent the travel path over the Portillo Rock Avalanche debris, and an internal friction angle of 35° was assumed representing a near-dry frictional rheology. The latter is characteristic of smaller rockslide and collapse events that fail as a series of partial detachments (e.g. the Randa rockslide; Eberhardt et al., 2004). The runout analysis results show that the bulk of the simulated flow is deposited proximally close to the base of the west slope (Fig. 15b). The rest of the flow continues moving several metres towards the SE and finally comes to rest generating a small ridge adjacent to the NNE margin of the deposit (Fig. 15c). This feature is in close agreement with a similar observable ridge in the actual S2 deposit (Fig. 15d).

6. Forward analysis of potential large-scale rockslide events at Portillo

The insights gained through the back analyses of the Portillo Rock Avalanche, with respect to the failure mechanism, problem geometry, rockslide rheology and rock mass and travel path properties, were subsequently used to develop and constrain forward analyses assessing the hazard potential of a reoccurring major rockslide (Fig. 16). Two triggering mechanisms were tested: that involving an elevated water table associated with a heavy precipitation event, and seismic loading to simulate a large earthquake event. As before, UDEC modelling was used to identify the potential failure mode and estimate the potential failed volume, and DAN3D was used to model the runout path of this failed volume (i.e. impact area) together with maximum velocities and deposit depths.

Table 6
Basal rheology and parameter values used in the DAN3D runout modelling of the Portillo Rock Avalanche event.

Property	Frictional	Voellmy
Applicable model elevation [m]	4050–2800	2800–2050
Basal friction, ϕ_b [°]	30	6
Pore fluid coefficient, r_u	0.18	n/a
Internal friction, ϕ_b [°]	35	n/a
Turbulence parameter, ζ [m/s^2]	n/a	500

6.1. Failure initiation

The UDEC models used to assess the Portillo rock slope's sensitivity to different triggering events were built using the present-day slope topography combined with the geology defined for the back analysis. Average to minimum properties based on those provided in Tables 4 and 5 were adopted. These models were time-stepped to an initial equilibrium, indicating a stable slope state even when lower bound rock mass and discontinuity properties were used. This agrees with the cosmogenic nuclide dating that indicates that the eastern slope has been stable for *ca.* 4.4 ka.

6.1.1. Modelled slope response to precipitation trigger

A rising water table was then added to the model. Although no field evidence was found indicating significant groundwater being present in the slope (e.g. seeps), this scenario was considered to test the response of the slope to a series of heavy prolonged precipitation events. Varying water tables were added assuming a moderately high water table coinciding with 3500 m.a.s.l. and a fully saturated slope condition with a water table at 4000 m.a.s.l. (Fig. 17a). The 3500 m.a.s.l. water table assumes that seepage is present but is occurring below the contact between the rock slope and overlying talus and is therefore not observable. The coupled hydro-mechanical steady-state fluid flow logic in UDEC was employed; fluid flow in UDEC is restricted to the fracture network (i.e. the blocks are impermeable) with a cubic law relationship being used to correlate fracture aperture to hydraulic conductivity. A tight joint aperture of 0.5 mm under zero normal stress decreasing to a minimum of 0.2 mm was assigned for the cross joints in the upper slope (Domain 1, JS2; Fig. 9), with the remaining joints being assigned a more open aperture of 5 mm under zero normal stress decreasing to a minimum of 2 mm. These were estimated based on field observations.

Results for the 3500 m.a.s.l. water table condition proved to be completely stable. A similar stable condition was observed for the

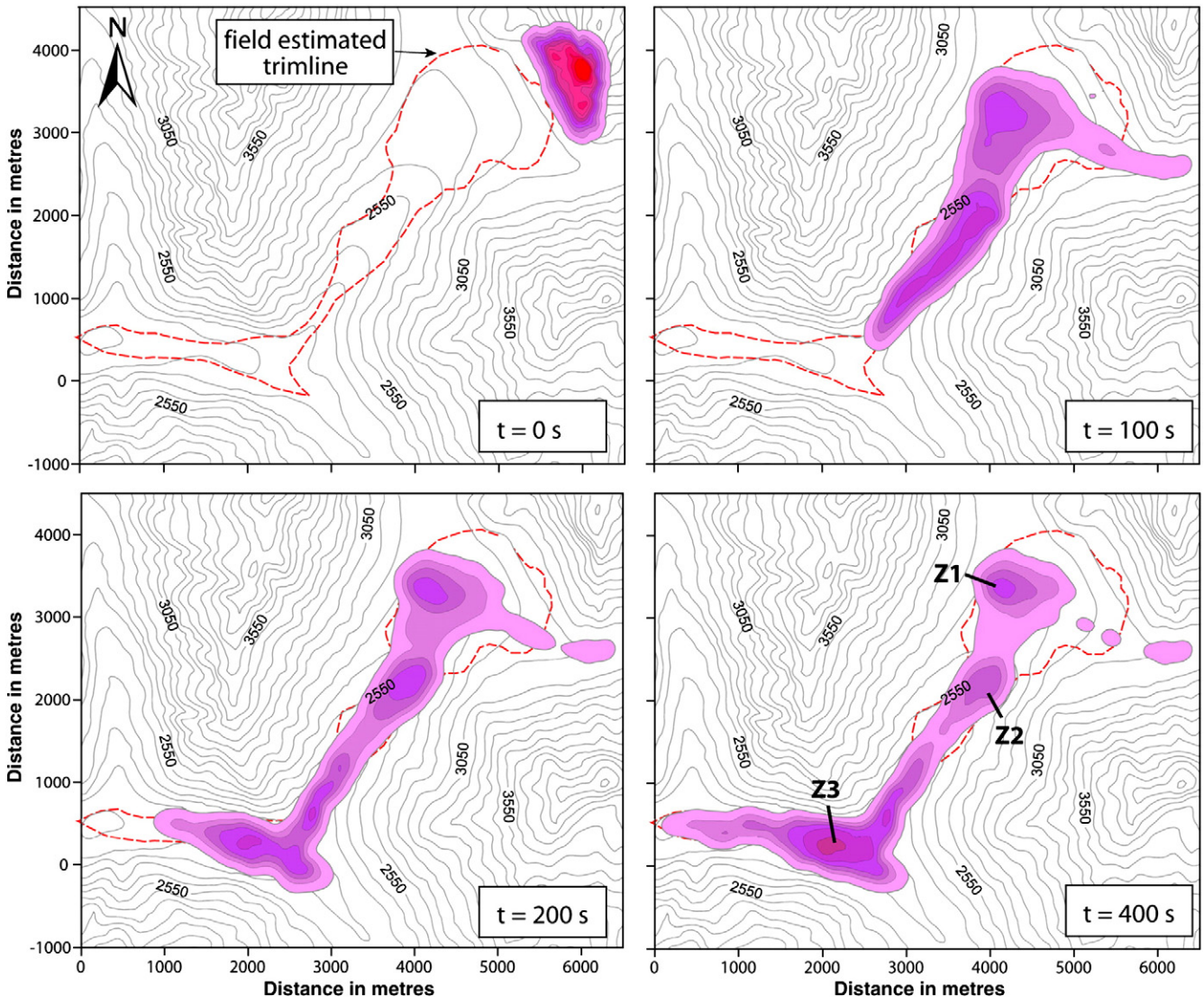

Fig. 14. DAN3D simulation of the Portillo Rock Avalanche event at various time intervals. The flow/deposit depth contours are at 10 m intervals and the elevation contours are at 100 m intervals. Superimposed is the field estimated trimline of the event.

worst case scenario of a fully saturated slope. Fig. 17b shows the results from this model. When plotting the plasticity indicators it is clear that a number of tensile damage indicators are present in the upper slope. These elements are directly related to the opening of joints due to the effect of increased joint water pressures. Similarly, a number of shear damage indicators appear in the weaker fault material of Domain 2, although not to the point that the stability of the slope is compromised in the model. When history points tracking the displacement of the toe are studied (Fig. 17c), they show that the slope reaches a stable equilibrium state. The lower apertures of the cross joints, and therefore the reduced drainage at the slope face, result in pore pressures in the bedding joints corresponding to a hydraulic head of approximately 100 m yet failure does not occur.

6.1.2. Modelled slope response to earthquake trigger

To assess the stability of the slope during a seismic event, a dynamic load was applied to the base of the UDEC model to simulate an earthquake trigger. A "quiet" boundary condition was assumed to simulate the free-field earthquake motion, meaning that plane waves propagating upwards are properly absorbed in the boundaries and suffer no distortion (Itasca, 2004). A critical component of the seismic analysis is the earthquake ground motion which is well defined by an acceleration time-history. Parameters such as peak ground acceleration (PGA), fundamental period (T_0), and effective duration (D_E; Bommer and Martinez-Pereira, 1999) may be used to characterize the intensity, dominant frequency, and duration of ground motion, respectively.

The earthquake event was simulated as a wave using a simple harmonic sinusoidal wave assuming a frequency, f, of 2.5 Hz, based on observations by Bhasin and Kaynia (2004) that measurements of seismic motions at rock slope sites are normally in the range of 2 to 5 Hz. The effective duration was calculated using the following relationship by Bommer and Martinez-Pereira (1999):

$$\mathrm{Log}(D_E) = 0,69M_W - 3.70. \quad (4)$$

This equation accounts for an earthquake ranging between moment magnitude $5 \leq M_w \leq 8$. The maximum ground particle velocity, υ, was calculated from Bhasin and Kaynia's (2004) relationship:

$$\upsilon = PGA / (2 \cdot \pi \cdot f). \quad (5)$$

The PGA range was obtained from seismic hazard maps for South America developed by Tanner and Shedlock (2004), accounting for a 2% chance of exceedance in 50 years for sites situated in rock. This corresponds to a 2475-year return period. Lastly, the excitation was

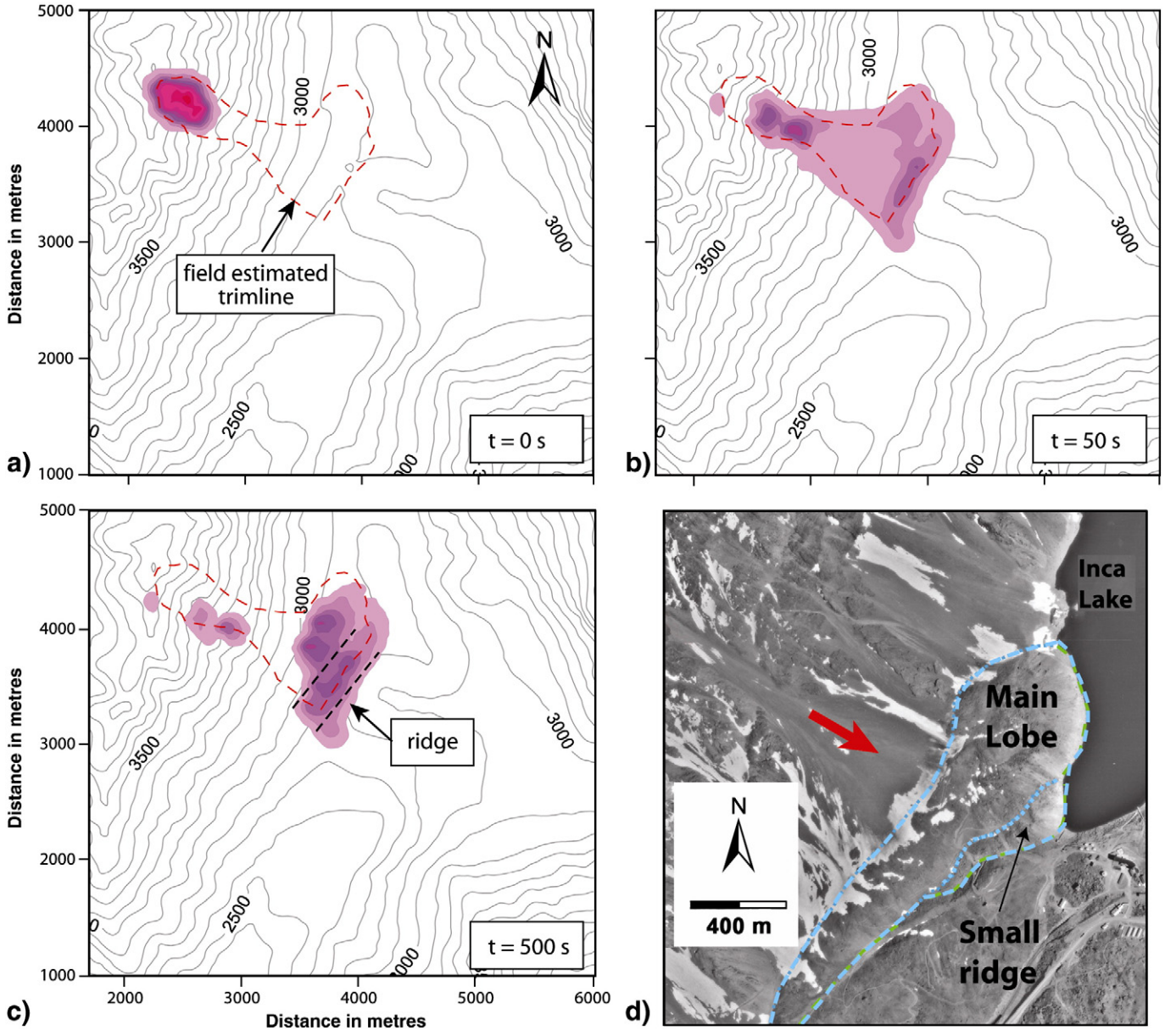

Fig. 15. DAN3D simulation of Holocene rockslide event showing flow depth contours (10 m intervals) at: a) $t = 0$ s, b) $t = 50$ s, and c) $t = 500$ s. Field estimated trimlines are shown as dashed lines. d) Aerial photograph (1:20,000) showing outline of the Holocene S2 deposit, including a small ridge to the southeast of main lobe.

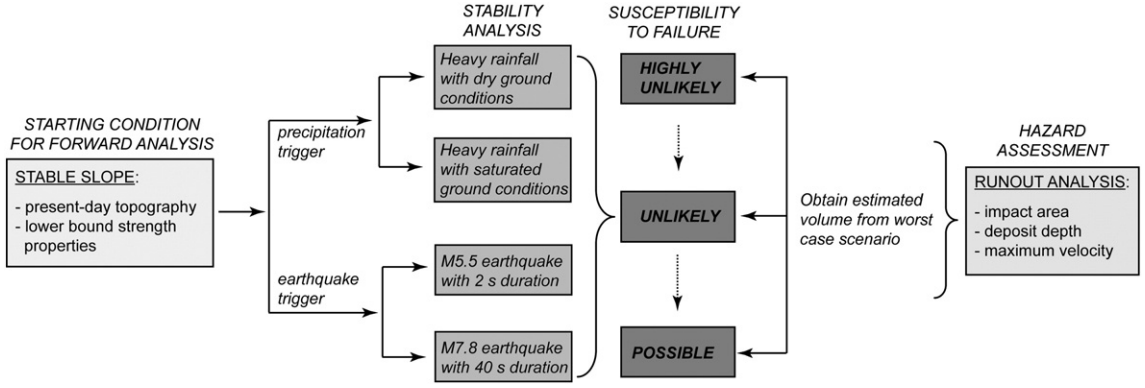

Fig. 16. Flow diagram showing the procedure followed and scenarios tested for the forward hazard assessment.

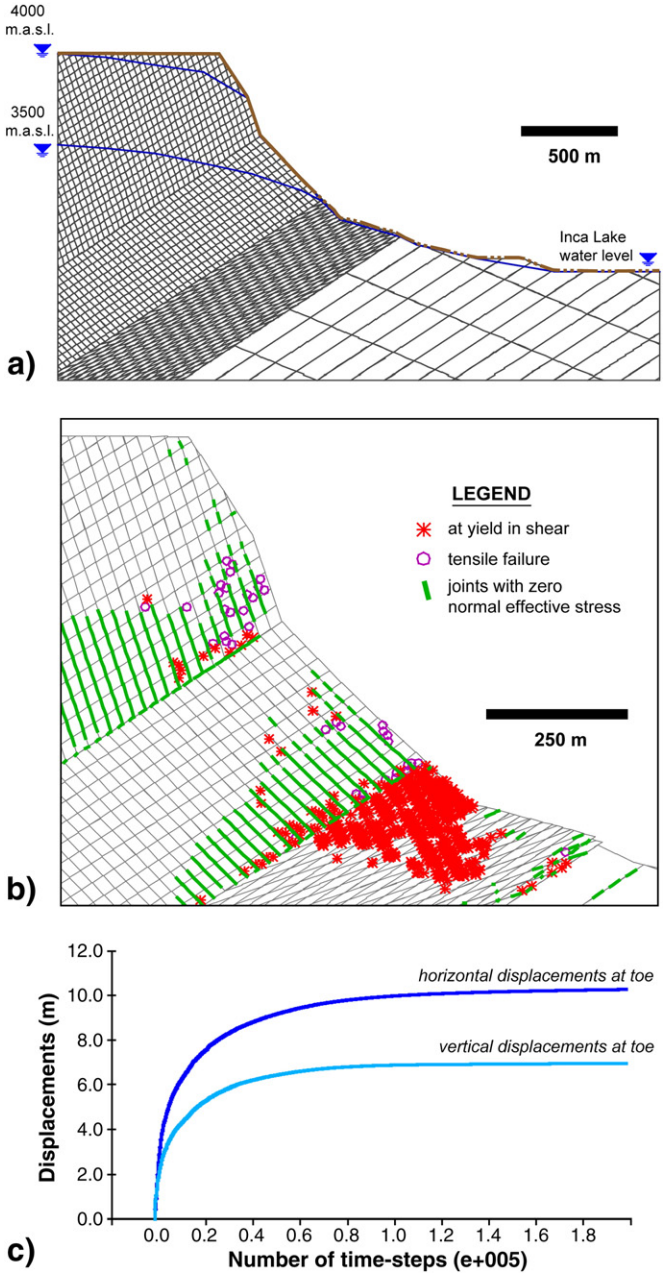

Fig. 17. Forward modelling of Portillo rock slope response to precipitation trigger, showing: a) UDEC model and simulated water tables; b) model results showing plasticity indicators; and c) history plot of displacements at toe of slope showing progression towards a stable state.

applied in the form of a shear stress using Eqs. (4) and (5), as specified by Itasca (2004):

$$\tau_s = 2(\rho \cdot v_s) \cdot \upsilon \tag{6}$$

$$v_s = (G/\rho)^{0.5} \tag{7}$$

where τ_s is the applied shear stress, ρ is the mass density, v_s is the speed of S-wave propagation through the rock mass, υ is the input shear particle velocity, and G is the shear modulus. The input variables used for the dynamic analysis are given in Table 7, with the lower bound values representing those that are characteristic of seismic events that have occurred in the Portillo region and the upper bound values representing a worst case scenario.

Table 7
Input parameters used for the UDEC dynamic analysis.

Parameter	Value range
Peak ground acceleration, PGA [% g, m/s^2]	0.8–1.2
Frequency, f [Hz]	2–5
Ground particle velocity, υ (m/s)	0.03–0.1
Shear wave velocity, v_s (m/s)	620–1360
Effective duration, D_E (s)	2–40
Shear stress, τ [MPa]	0.1–0.7

Model results using input values based on earthquake magnitudes and durations observed in the Portillo region ($M_w = 5.5$) did not result in the triggering of a catastrophic rockslide in the model. This agrees with the non-occurrence of large failures during earthquakes in historic times. The most pronounced effect was an increased number of blocks in the upper slope yielding in tension (Fig. 18a), which may correspond with small volume rock fall episodes loosened by the earthquake. Fig. 18b shows the response of the Caracoles Range slope using input values equivalent to a $M_w = 7.8$ earthquake. Analysis of the plasticity indicators shows that unlike the back analysis of the Portillo Rock Avalanche, where failure initiated at the toe of the slope in shear, failure in tension dominates along the slope face. Topographic amplification, involving the focusing of seismic waves due to the convex topography (Assimaki and Gazetas, 2004), appears to be a factor. When velocity vectors are overlaid (Fig. 18b inset), both indicators suggest the development of an outward rotation and collapse of blocks along the crest of the slope. The corresponding slide volume for this failure would be in excess of 1 million m^3, assuming a maximum length for the scarp between 50 and 100 m based on topographic constraints. The elements that yield in tension below the hinge probably represent unravelling of the lower portion of slope associated with some degree of buckling. Close to the base of the slope, tensile failure and large displacements (i.e. heaving) occur due to the dilation of the weaker zone of damaged rock.

6.2. Runout analysis of failed volume

The failed volume obtained for the earthquake-triggered slide below the crest of the slope was increased by 25% to account for bulking of the failed mass due to fragmentation. This volume was then used as an input condition for a runout analysis, for which two scenarios concerning the travel path conditions were assumed: failure occurs during the dry season and must override previously deposited and non-saturated, highly frictional debris (i.e. talus and debris belonging to the Portillo Rock Avalanche and Holocene rockslides); and failure occurs in a wet season, where the talus and debris along the path are covered by a deep snow. A frictional rheology (basal friction = 30°, internal friction = 35°, and pore-fluid pressure coefficient, $r_u = 0.18$) and a Voellmy rheology (basal friction = 6° and turbulence = 500 m/s^2) were used for these two scenarios, respectively, based on those calibrated from the back analysis of the Portillo Rock Avalanche.

For the frictional case, corresponding to dry conditions, the leading edge of the flow runs over part of the International Santiago–Mendoza Corridor and stops in a flat area in the upper part of the valley, depositing between 1 and 12 m of debris (Fig. 19a). For this simulation there is no direct indication of material impacting the ski resort facilities, as most of the debris accumulates to the south within the local drainage basin. Nevertheless, given the close proximity of the leading edge of the runout debris to the resort hotel, a minor amount of debris may impact it in the form of outlying boulders and rock debris.

For the second case, accounting for the slide debris overriding and entraining snow, the results show the flow separating with the lobe to the south carrying most of the volume (Fig. 19b). This path is spatially

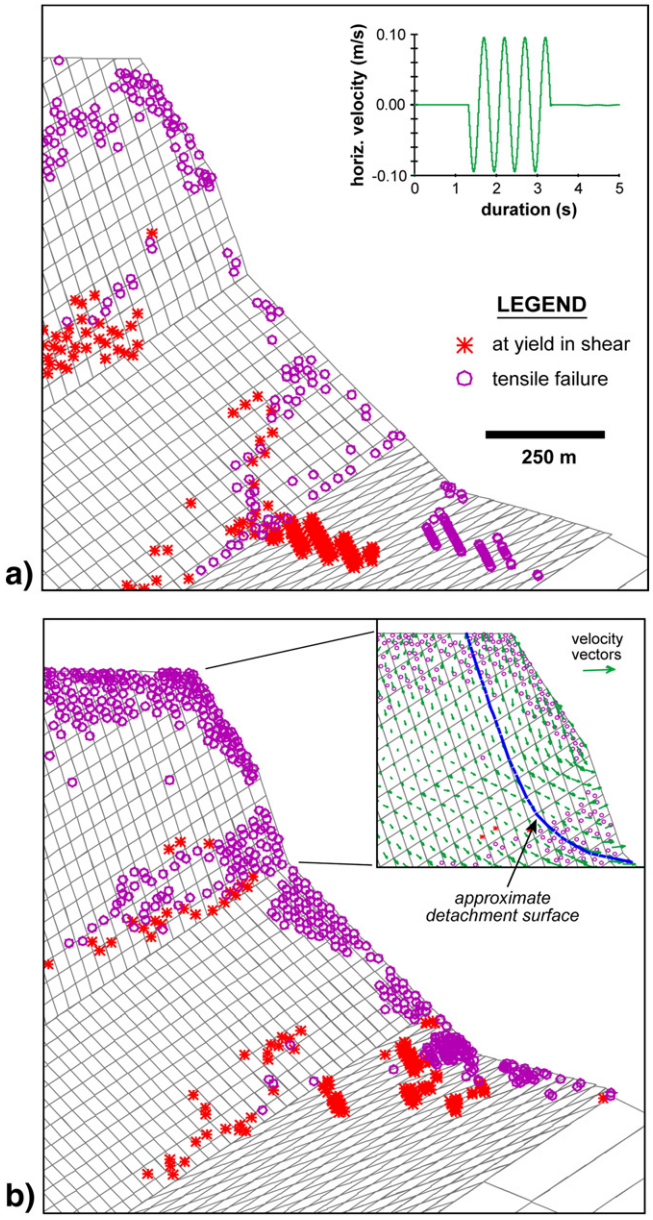

Fig. 18. Forward UDEC modelling of Portillo rock slope response to an earthquake trigger, showing: a) results for a $M_w = 5.5$ earthquake showing plasticity indicators and ground response to dynamic loading in the form of horizontal velocities (inset); and b) results for a $M_w = 7.8$ earthquake showing plasticity indicators and velocity vectors outlining projected detachment surface (inset).

related to the drainage network (i.e. topographic lows). The leading edge in this case reaches approximately 90 m further than the first scenario, as would be expected given the increased mobilised behaviour resulting from the entrained snow. In general terms, this simulation clearly highlights the sensitivity of the Voellmy rheology to the path topography. Both simulations show that the maximum velocities are reached towards the southern limit of the deposits (Fig. 19c,d), which coincides with the local river channel. This result is important because if a larger volume is involved, the potential reach and impact of the runout increases down the valley.

7. Conclusions

A conclusive statement regarding the Portillo Rock Avalanche and the Holocene rockslides from opposite valley walls is unlikely due to the number of uncertainties inherent with back analyzing prehistoric slope failure events. However, the use of numerical simulation tools combined with geological mapping, field observations and engineering judgment, enabled significant insights to be gained to unravel the complex geological history in rockslide-prone valleys like Portillo and to later extend these results to hazard assessments of future rockslide events. The hazard assessment framework followed linking back and forward analyses of rockslide initiation and runout processes, proved to be an effective means towards developing an overall understanding of the hazard level posed by the present-day rock slope conditions.

Cosmogenic nuclide dating together with detailed geologic and geomorphologic mapping helped constrain the origin of the valley deposits below the Caracoles Range. The chronology of events set them in a post-glacial period, clustered around 13.4 and 4.4 ka, thus ruling out a glacial origin for any of the lobes. The use of discontinuum numerical modelling techniques (i.e. UDEC) applied in the analysis of the Portillo Rock Avalanche supported the field observations with respect to the most probable failure mechanism. A stress-controlled failure at the toe of the slope represented by shearing of the rock mass continuum enabled a structurally controlled failure in the upper part of the slope by means of sliding and shearing along bedding planes. The resulting model also provided new insights into the way the slide mass failed, suggesting the possibility of a staged failure through an active–passive Prandtl wedge. The lack of daylighting discontinuities dipping shallowly out of the slope and the non-sensitivity of the modelled failure mechanism to variations in rock mass and discontinuity strength parameters, strongly suggests a failure mode controlled by the steep dipping bedding planes combined with back-thrust structures at the toe of the slope. Several possibilities could be mentioned that might have helped or triggered the slope failure, the most important being:

- glacial rock mass damage which led to progressive failure mechanisms, both in the form of asperity breakdown along the bedding planes and loss of coherence in the stronger units at the toe of the slope through brittle fracture processes, attributed to shearing of the valley sides by the ice-sheet that advanced along the valley floor;
- glacial oversteepening of the valley walls during glacial advance and debuttressing of the paleoslope during glacial retreat (i.e. after the LGM, approximately 14.5 ka); and
- an exceptionally large-magnitude earthquake.

The use of DAN3D in the dynamic analysis proved to be a powerful tool for modelling rockslide runouts, with insights being provided that agreed with field observations in a number of ways. The formation of Inca Lake arising through the blocking of the natural valley drainage system due to the debris of the Portillo Rock Avalanche is almost certain. In addition, the model results appear to discount the possibility of the two Holocene deposits found at the bottom of the east and west facing slopes as originating from a single source. Instead, it is more likely that they were formed through two rock slope failure events, one from the eastern slope and one from the western slope, perhaps temporally linked to the same triggering event (e.g. a large earthquake). Accordingly, the runout models support the interpretation of the chronological distribution of the deposits, based on the cosmogenic nuclide dating by ^{36}Cl.

The forward modelling helped in the assessment of the potential hazard posed by the eastern slope to the Portillo site. The static and dynamic conditions under which the slope was tested suggest that the present-day stability of the eastern slope under static conditions, even when assuming low rock mass and discontinuity strength properties, is probably the product of a more stable slope profile following the prehistoric Portillo Rock Avalanche event. Coupled hydro-mechanical modelling results indicate that even if fully saturated, the slope would remain stable. The nature of the bedding and fracture permeability network for which the water pressures would be concentrated at the

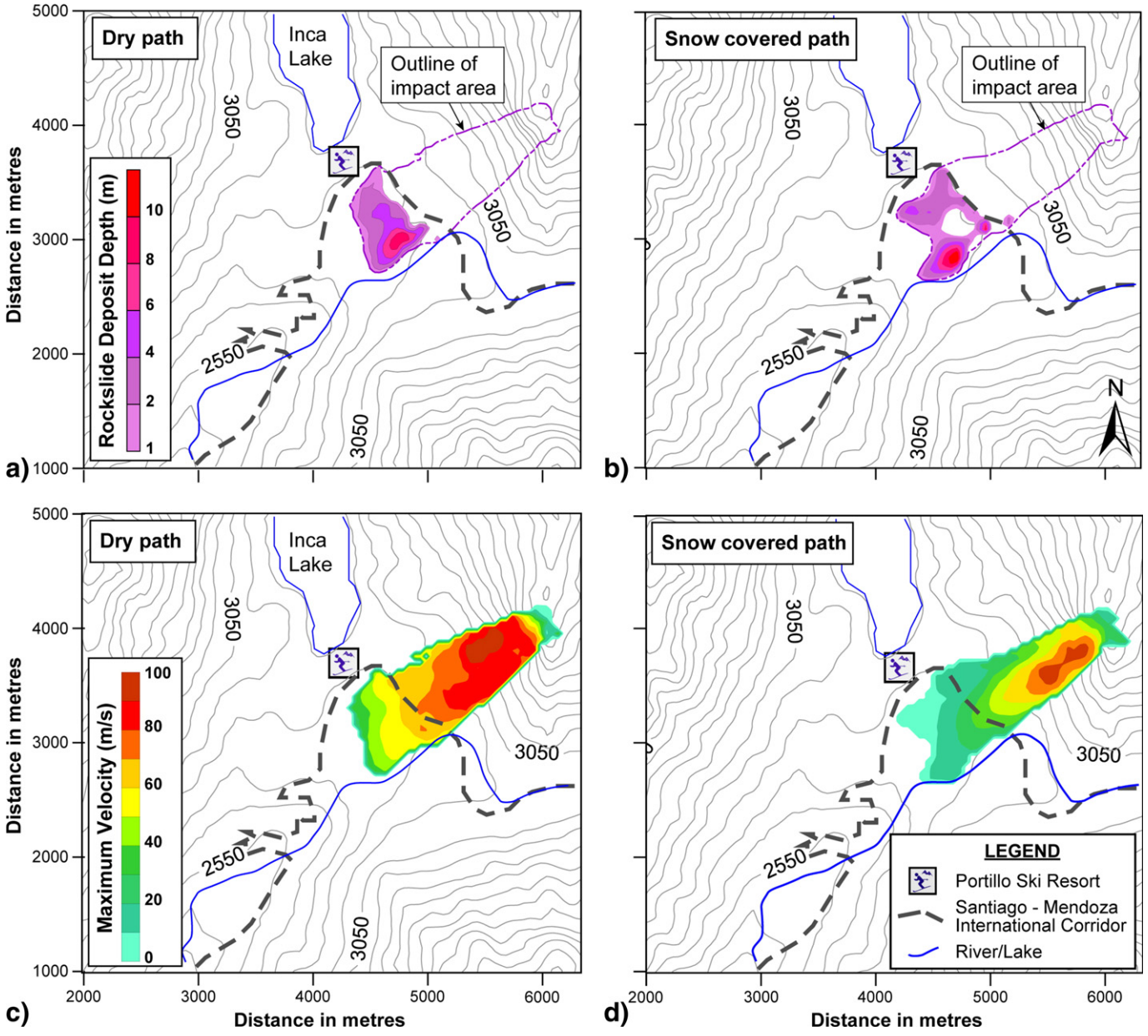

Fig. 19. DAN3D runout assessment of earthquake-triggered rockslide originating at the crest of the slope. a,b) Maximum depth of the deposit assuming a dry, frictional path and a path covered with deep snow, respectively. c,d) Maximum rockslide velocities for the same two scenarios.

toe of the slope, still did not produce an unstable condition exceeding the rock mass effective strength.

However, the modelling results did indicate the potential for a failure to develop in the present-day slope in the event of a high magnitude ($M_w = 7.8$) earthquake with its epicentre near or below the slope. The modelled effects of the seismic loading resulted in the instability of the crest of the slope, probably augmented by topographic amplification. The estimated volume of the potential slide was 1 million m^3. The results of a DAN3D runout analysis based on this volume suggest that the leading edge of the flow could override part of the International Santiago–Mendoza Corridor, regardless of whether the travel path over talus and rockslide debris was dry or covered by snow. The Portillo Ski Resort does not appear to be directly impacted by the flow debris; however its close proximity with the edge of the deposit may result in some damage to the structure. Despite this finding, it must be emphasized that an earthquake of this magnitude has not been recorded in the Portillo region, thus the nature of the hazard is low.

Acknowledgments

The authors would like to acknowledge the Geological and Mining Survey of Chile (SERNAGEOMIN), Geological Survey of Canada (GSC) and Multinational Andean Project (MAP:GAC) for providing funding and logistical support for the field work and Cosmogenic Nuclide dating work carried out. Laboratory testing was carried out in the UBC Mining Rock Mechanics laboratory with the assistance of Cristián Cáceres, and in the UBC Earth and Ocean Sciences Petroleum Geomechanics Laboratory with the assistance of Dr. Laxmi Chikatamarla. The authors would also like to thank Drs. Oldrich Hungr and Scott McDougall for their assistance with the DAN3D modelling and numerous insights during the course of this work. The Optech laser scanner was acquired through an NSERC Equipment Grants, with additional funding being provided through an NSERC Discovery grant. Support for this work was also provided in part by the Research Council of Norway through the International Centre for Geohazards (ICG). Their support is gratefully acknowledged. This is ICG contribution No. 290.

References

Antinao, J.L., Gosse, J., 2009. Large rockslide in the Southern Central Andes of Chile (32–34.5°S): tectonic control and significance for Quaternary landscape evolution. Geomorphology 104, 117–133.

Assimaki, D., Gazetas, G., 2004. Soil and topographic amplification on canyon banks and the 1999 Athens earthquake. Journal of Earthquake Engineering 8 (1), 1–43.

Ballantyne, C.K., Stone, J.O., Fifield, L.K., 1998. Cosmogenic Cl-36 dating of postglacial landsliding at The Storr, Isle of Skye, Scotland. Holocene 8 (3), 347–351.

Barrientos, S., Vera, E., Alvarado, P., Monfret, T., 2004. Crustal seismicity in central Chile. Journal of South American Earth Sciences 16 (8), 759–768.

Barton, N., 1972. A model study of rock-joint deformation. International Journal of Rock Mechanics and Mining Sciences & Geomechanics Abstracts 9 (5), 579–602.

Bhasin, R., Kaynia, A.M., 2004. Static and dynamic simulation of a 700-m high rock slope in western Norway. Engineering Geology 71 (3–4), 213–226.

Bieniawski, Z.T., 1989. Engineering Rock Mass Classifications: A Complete Manual for Engineers and Geologists in Mining, Civil, and Petroleum Engineering. John Wiley, New York. 272 pp.

Bommer, J., Martinez-Pereira, A., 1999. The effective duration of earthquake strong motion. Journal of Earthquake Engineering 3 (2), 127–172.

Cahill, T., Isacks, B., 1992. Seismicity and shape of the subducted Nazca Plate. Journal of Geophysical Research 97 (B12), 17503–17529.

Caviedes, C., Paskoff, R., 1975. Quaternary glaciations in the Andes of north-central Chile. Journal of Glaciology 14 (70), 155–170.

Charrier, R., Baeza, O., Elgueta, S., Flynn, J.J., Gana, P., Kay, S.M., Muñoz, N., Wyss, A.R., Zurita, E., 2002. Evidence for Cenozoic extensional basin development and tectonic inversion south of the flat-slab segment, southern Central Andes, Chile (33°–36° S.L.). Journal of South American Earth Sciences 15 (1), 117–139.

Coggan, J.S., Stead, D., Eyre, J., 1998. Evaluation of techniques for quarry slope stability assessment. Transactions of the Institute of Mining and Metallurgy, Section B: Applied Earth Sciences 107, B139–B147.

Corominas, J., 1996. The angle of reach as a mobility index for small and large landslides. Canadian Geotechnical Journal 33 (2), 260–271.

Costa, C.H., Gonzalez-Diaz, E.F., 2007. Age constraints and paleoseismic implication of rock avalanches in the northern Patagonian Andes, Argentina. Journal of South American Earth Sciences 24 (1), 48–57.

Dunne, J., Elmore, D., Muzikar, P., 1999. Scaling factors for the rates of production of cosmogenic nuclides for geometric shielding and attenuation at depth on sloped surfaces. Geomorphology 27 (1), 3–11.

Eberhardt, E., Stead, D., Coggan, J.S., 2004. Numerical analysis of initiation and progressive failure in natural rock slopes — the 1991 Randa rockslide. International Journal of Rock Mechanics & Mining Sciences 41 (1), 69–87.

Fisher, B.R., Eberhardt, E., 2007. Numerical modeling and shear strength estimates of biplanar dip slope failures. In: Sousa, Ribeiro e, et al. (Ed.), Proceedings of the 11th Congress of the International Society for Rock Mechanics, Lisbon, 9–13 July 2007. Taylor & Francis, London, pp. 633–636.

Giambiagi, L.B., Ramos, V.A., 2002. Structural evolution of the Andes in a transitional zone between flat and normal subduction (33°30′–33°45′S), Argentina and Chile. Journal of South American Earth Sciences 15 (1), 101–116.

Godoy, E., 1994. Derrumbes de Cerros Holocenos en los Andes Centrales de Chile. Proceedings of the 7th Chilean Geological Conference, Concepcion, Chile, Vol.1, pp. 310–314.

Godoy, E., 2002. Remociones en masa de aspecto Cuaternario en el frente tectonico cordillerano de Chile central, los depositos de Colo-Coya y Gualtatas, Chile. International Symposium of Environmental Geology for Land Use Planning, Puerto Varas, Chile, Vol. 1, pp. 58–61.

Godoy, E., Yañez, G., Vera, E., 1999. Inversion of an Oligocene volcano-tectonic basin and uplifting of its superimposed Miocene magmatic arc in the Chilean Central Andes: first seismic and gravity evidences. Tectonophysics 306 (2), 217–236.

Gosse, J.C., Phillips, F.M., 2001. Terrestrial in situ cosmogenic nuclides: theory and application. Quaternary Science Reviews 20 (14), 1475–1560.

Hermanns, R.L., Niedermann, S., Villanueva-Garcia, A., Sosa-Gomez, J., Strecker, M.R., 2001. Neotectonics and catastrophic failure of mountain fronts in the southern intra-Andean Puna Plateau, Argentina. Geology 29 (7), 619–623.

Hermanns, R.L., Niedermann, S., Ivy-Ochs, S., Kubik, P.W., 2004. Rock avalanching into a landslide-dammed lake causing multiple dam failure in Las Conchas valley (NW Argentina) — evidence from surface exposure dating and stratigraphic analyses. Landslides 1 (2), 113–122.

Hoek, E., Kaiser, P.K., Bawden, W.F., 1995. Support of Underground Excavations in Hard Rock. Balkema, Rotterdam. 215 pp.

Hoek, E., Carranza-Torres, C.T., Corkum, B., 2002. Hoek-Brown failure criterion — 2002 edition. In: Hammah, et al. (Ed.), Proceedings of the Fifth North American Rock Mechanics Symposium (NARMS-TAC), Toronto, 7–10 July 2002. University of Toronto Press, pp. 267–273. vol. 1.

Hungr, O., Evans, S.G., 1996. Rock avalanche runout prediction using a dynamic model. In: Senneset (Ed.), Proceedings of the 7th International Symposium on Landslides, Trondheim, Norway, 17–21 June, 1996. A.A. Balkema, Rotterdam, pp. 233–238.

Hungr, O., Evans, S.G., 2004. Entrainment of debris in rock avalanches; an analysis of a long run-out mechanism. Geological Society of America Bulletin 116 (9/10), 1240–1252.

Hungr, O., Corominas, J., Eberhardt, E., 2005. Estimating landslide motion mechanism, travel distance, and velocity. In: Hungr, et al. (Ed.), Landslide Risk Management. Taylor and Francis, London, pp. 99–128.

Itasca, 2004. UDEC: User's Guide (Version 4.0). Itasca Consulting Group, Inc, Minneapolis.

Jaboyedoff, M., Baillifard, F., Couture, R., Locat, J., Locat, P., 2004. Toward preliminary hazard assessment using DEM topographic analysis and simple mechanical modeling by means of sloping local base level. In: Lacerda, et al. (Ed.), Proceedings of the 9th International Symposium on Landslides and Engineered Slopes, Rio de Janeiro, 28 June–2 July, 2004. A.A. Balkema, Leiden, pp. 199–205. Vol.1.

Keefer, D.K., 1984. Landslides caused by earthquakes. Geological Society of America Bulletin 95 (4), 406–421.

Kimber, O.G., Allison, R.J., Nicholas, J.C., 1998. Mechanisms of failure and slope development in rock masses. Transactions of the Institute of British Geographers, New Series 23 (3), 353–370.

Kulhawy, F.H., 1975. Stress deformation properties of rock and rock discontinuities. Engineering Geology 9 (4), 327–350.

Kvapil, R., Clews, K.M., 1979. An examination of the Prandtl mechanism in large-dimension slope failures. Transactions of the Institute of Mining and Metallurgy, Section A: Mining Industry 88, A1–A5.

Li, T., 1983. A mathematical model for predicting the extent of a major rockfall. Zeitschrift für Geomorphologie 27 (4), 473–482.

Lomnitz, C., 1961. Los terremotos del 4 de Septiembre en el Cajon del Maipo. Anales de la Facultad de Ciencias Fisicas y Matematicas 3 (18), 279–306.

Marinos, V., Marinos, P., Hoek, E., 2005. The geological strength index: applications and limitations. Bulletin of Engineering Geology and the Environment 64 (1), 55–65.

McDougall, S. 2006. A new continuum dynamic model for the analysis of extremely rapid landslide motion across complex 3-D terrain. Ph.D. Thesis, University of British Columbia, Vancouver.

McDougall, S., Hungr, O., 2004. A model for the analysis of rapid landslide motion across three-dimensional terrain. Canadian Geotechnical Journal 41 (6), 1084–1097.

McDougall, S., Pirulli, M., Hungr, O., Scavia, C., 2008. Advances in landslide continuum dynamic modeling. In: Chen, et al. (Ed.), Proceedings of the 10th International Symposium on Landslides and Engineered Slopes, Xi'an, China, 30 June–4 July 2008. CRC Press, London, pp. 145–157. vol. 1.

Mencl, V., 1966. Mechanics of landslides with non-circular slip surfaces with special reference to the Vaiont slide. Geotechnique 16 (4), 329–337.

Olsson, R., Barton, N., 2001. An improved model for hydromechanical coupling during shearing of rock joints. International Journal of Rock Mechanics and Mining Sciences 38 (3), 317–329.

Pardo, M., Comte, D., Monfret, T., 2002. Seismotectonic and stress distribution in the central Chile subduction zone. Journal of South American Earth Sciences 15 (1), 11–22.

Phillips, F.M., Plummer, M.A., 1996. CHLOE: a program for interpreting in situ cosmogenic nuclide data for surface exposure dating and erosion studies. Radiocarbon 38, 98–99.

Priest, S.D., 1993. Discontinuity Analysis for Rock Engineering. Chapman & Hall, London. 473 pp.

Ramos, V.A., Zapata, T., Cristallini, E., Introcaso, A., 2004. The Andean Thrust system — latitudinal variations in structural styles and orogenic shortening. In: McClay, K.R. (Ed.), Thrust Tectonics and Hydrocarbon Systems: AAPG Memoir, Vol. 82, pp. 30–50.

Rivano, G.S., Sepúlveda, H.P., Boric, P.R., Espiñeira, T.D., 1993. Mapa Geológico de la Hoja Quillota-Portillo (escala 1:250.000), V Región de Valparaíso. Carta Geológica de Chile, No. 73. Servicio Nacional de Geología y Minería, Santiago.

Scheidegger, A., 1973. On the prediction of the reach and velocity of catastrophic landslides. Rock Mechanics 5 (4), 231–236.

Sepulveda, S.A., Astroza, M., Kausel, E., Campos, J., Casas, E., Rebolledo, S., Verdugo, R., 2008. New findings on the 1958 Las Melosas earthquake sequence, central Chile: Implications for seismic hazard related to shallow crustal earthquakes in subduction zones. Journal of Earthquake Engineering 12 (3), 432–455.

Stead, D., Eberhardt, E., Coggan, J.S., 2006. Developments in the characterization of complex rock slope deformation and failure using numerical modelling techniques. Engineering Geology 83 (1–3), 217–235.

Strouth, A., Eberhardt, E., 2009. Integrated back and forward analysis of rock slope stability and rockslide runout at Afternoon Creek, Washington. Canadian Geotechnical Journal 46 (10), 1116–1132.

Tanner, J.G., Shedlock, K.M., 2004. Seismic hazard maps of Mexico, the Caribbean, and Central and South America. Tectonophysics 390 (1–4), 159–175.

Tebbens, S.F., Candie, S.C., 1997. Southeast Pacific tectonic evolution from early Oligocene to present. Journal of Geophysical Research 102 (6), 12061–12084.

Wyllie, D.C., Mah, C.W., 2004. Rock Slope Engineering: Civil and Mining (4th Edition). Spon Press, New York. 431 pp.

Yañez, G., Cembrano, J., Pardo, M., Ranero, C., Selles, D., 2002. The Challenger–Juan Fernandez–Maipo major tectonic transition of the Nazca-Andean subduction system at 33–34°S: geodynamic evidence and implications. Journal of South American Earth Sciences 15 (1), 23–38.